A Real-time Robust Method for Post-disaster Load Restoration of Coordinated Power-Transportation System with Vehicle-to-grid Response

Houbo Xiong, *Student Member*, *IEEE*, Yan Xu, *Senior Member*, *IEEE*, Zhao Yang Dong, *Fellow*, *IEEE*, Wei Gan, *Member*, *IEEE*, Chuangxin Guo, *Senior Member*, *IEEE*, Mingyu Yan, *Member*, *IEEE*

***Abstract*—With the proliferation of electric vehicles (EVs), vehicle-to-grid (V2G) capability emerges as a potential resource for load restoration after a large disruption. This paper presents a real-time post-disaster load restoration method for the coordinated power distribution networks (PDN) and urban traffic networks (UTN) with V2G response. The multi-period restoration problem is modeled as a dynamic programming-based multi-stage robust optimization model, addressing uncertainties of renewable generation and traffic demands. It incorporates a dynamic traffic assignment scheme to characterize vehicle travels and V2G services within short time slots. Then, an improved robust dual dynamic programming algorithm is proposed to solve the multi-stage robust optimization problem. For online application, the solved value functions from each stage serve as per-period policies, leveraging knowledge of future uncertainties to quickly guide real-time load restoration through distributed resource dispatch, network reconfiguration, and V2G assignments. Numerical experiments with a 33-bus PDN and 20-road UTN, plus a real-world 91-bus PDN with 35-road UTN, validate the effectiveness of proposed restoration method.**

***Index Terms*—Vehicle-to-grid, power-transportation system, post-disaster real-time restoration, dynamic traffic flow, multi-stage optimization, uncertainties.**

Nomenclature

Indices and Sets

$g\in\mathcal{G}$, $d\in\mathcal{D}$	Set of DG, set of loads
$w\in\mathcal{W}$, $i\in\mathcal{I}$	Set of DRE, set of PDN bus
$ij\in\mathcal{L}^{+/-(i)}$	Set of PDN lines from/to bus i
$k\in\mathcal{K}_{b/h}$	Set of UTN path containing road b/node h
$h\in\mathcal{H}^{(c)}$	Set of UTN node (with FCS)
$b\in\mathcal{B}$, $t\in\mathcal{T}$	Set of UTN road, set of time intervals
$rs\in\mathcal{O}$	Set of O-D pairs
u/o	Superscript for EVs supporting V2G response or not
$m\in\mathcal{M}$	Set of island subsystems after reconfiguration
$s\in S_t$	Set of valid iterations and sample points at stage t

Parameters

c^{sd}, c^{ul}	Penalties of load shedding, DRE curtailment
r^{tv}, $\mu^{cm}_{h,t}$	Coefficient of traveling and V2G compensation
V, $R_g^{+(-)}$	Nominal voltage magnitude, DG ramp limitation
ω_d	Critical ratio of load d
ϕ_i	Root bus indicator, if a DG is located to i, $\phi_i = 1$
r_{ij}, x_{ij}	Resistance and reactance in line ij
$L(Q)D_{d,t}$	(Re)Active load demand of load d at period t
$tan\varphi_{w/h}$	Power factor for DRE w or FCS located to node h
$f_{rs,t}$	Forecast traffic demand for O-D pair rs at period t
$Ar_{w,t}$	Forecast available power of DRE w at period t
$\wp_b$, Γ_h	Capacity of road b and FCS in node h
N^{sp}	Limitation of switch operation times
t_b^0, Δp	Travel time of road a, factor for EV flow to power
$\overline{(\cdot)}$, $\underline{(\cdot)}$	Upper/lower output limit of equipment $(\cdot)$

Variables

$Yl_{ij,m,t}$	Binary statues for line ij whether in subsystem m
$Yn_{i,m,t}$	Binary statues for bus i whether in subsystem m
$Yf_{ij,t}$, $Gt_{i,t}$	Unit commodity on line ij and generated from bus i
$v^{op/cl}_{ij,t}$	Binary statues for open/close of switch in line ij
$P(Q)d_{g,t}$	(Re)Active output of DG g at period t
$V_{i,t}$	Voltage magnitude in bus i at period t
$\partial V_{ij,t}$	Auxiliary variable for voltage magnitude
$P(Q)r_{w,t}$	(Re)Active output of DER e at period t
$P(Q)f_{ij,t}$	(Re)Active power flow in line ij at period t
$P(Q)vg_{h,t}$	(Re)Active V2G power to FCS in node h at period t
$Ls_{d,t}$	Shedding power of load d at period t
$u_{b,k,t}$, $q_{b,k,t}$	Inflow and outflow of road b, path k at period t
$x^{qd}_{b,k,t}$, $x^{ge}_{b,k,t}$	Queue/total EV flow in road b, path k at period t
$y_{h,k,t}$, $z_{h,k,t}$	Inflow and outflow of node h, path k at period t
$y^{cs}_{h,k,t}$, $z^{cs}_{h,k,t}$	Inflow and outflow of FCS in node h at period t
$x^{qu}_{h,k,t}$, $x^{sv}_{h,k,t}$	Queue and service flow of FCS in node h, period t
$y^{sv}_{h,k,t}$, $z^{fr}_{h,k,t}$	Service/free inflow in FCS in node h at period t
$\xi_{w,t}$, $\varsigma_{rs,t}$	Forecast error for DRE power and traffic demand

I. Introduction

With the proliferation of EVs supporting the zero-carbon transition, numerous fast charging stations (FCSs) have been established, affecting both power flow in power distribution networks (PDN) and traffic flow in urban traffic networks (UTN) [1]. This deepens the coupling between PDN and UTN, where coordinated operation has shown economic and flexible benefits [2], [3]. As natural

This work was supported by the State Key Program of National Natural Science Foundation of China (U22B2098) and (52307100). H. Xiong, C. Guo, are with the College of Electrical Engineering in Zhejiang University, Hangzhou, Zhejiang, 310013, China. (e-mail: houboxiong@zju.edu.cn, guochuangxin@zju.edu.cn). Y. Xu is with the School of Electrical and Electronic Engineering, Nanyang Technological University, Singapore 639798, email: xuyan@ntu.edu.sg. Z. Y. Dong are with the Department of Electrical Engineering, City University of Hong Kong, Hong Kong (email: zydong@ieee.org). W. Gan is with the School of Engineering, Cardiff University, CF24 3AA Cardiff, U.K. (e-mail: ganw4@cardiff.ac.uk). M. Yan is with the School of Electrical and Electronic Engineering, Huazhong University of Science and Technology, Wuhan 430073, China (e-mail: mingyuyan@hust.edu.cn). *(Corresponding author: Chuangxin Guo; Mingyu Yan)*

disasters become more frequent and severe [4], resilient coordination of PDN and UTN during extreme events is crucial [5], especially for post-disaster restoration. Developing a real-time load restoration strategy is essential to quickly serve critical users and provide emergency power for key transportation components like traffic control systems.

For load restoration in coupled PDN and UTN systems, while implementing distributed resource dispatch and network reconfiguration in PDN, many studies utilize mobile energy storage in UTN to actively support underpowered PDN buses [6]-[7]. With the advent of vehicle-to-grid (V2G) technology, electric vehicles (EVs) have also emerged as potential mobile resources. Some studies [8]-[10], propose using EVs for PDN load restoration via V2G. However, these studies [6]-[10] often overlook the coordinated assignment and congestion issues of emergency devices or V2G EVs with regular vehicles based on UTN road parameters and origin-destination (O-D) traffic demand. Recent works in Refs. [11] address the coordinated assignment of V2G-participating EVs with other vehicles but enforce changes to the EVs' travel destinations. In fact, EV owners with sufficient power should be able to opt for V2G response en route without altering their travel plans, incentivized by earning compensations. Moreover, existing relevant methods are computationally intensive, primarily focusing on day-ahead deployment or scheduling strategies, with few supporting rapid real-time restoration.

In the real-time operation of coordinated PDN and UTN, most studies use a rolling horizon scheme known as model predictive control (MPC) to manage computational demands [12], [13], [14]. To manage uncertainties like distributed renewable energies (DRE), several studies have integrated two-stage stochastic optimization (SO) and robust optimization (RO) with MPC method [15]. While MPC-based methods employing mobile emergency generators explored in [12], introducing EVs as real-time restoration resources adds significant complexity. This complexity arises from the real-time need to manage congestion, queuing, and EV services in UTN within shorter time intervals, typically less than 15 minutes, necessitating a dynamic traffic assignment (DTA) model. Unlike the static [2], [6], [11] and semi-dynamic [3] traffic assignment models, commonly used in day-ahead strategies, the DTA model accommodates UTN dynamics more effectively but is more complex to implement. The characteristics of different traffic assignment models are summarized and compared in Table I. Although recent study [5] introduced a resilient scheduling model for integrated PDN and UTN under extreme events using the DTA model, it lacks support for real-time computation and does not consider V2G as restoration resources.

TABLE I
FEATURES OF DIFFERENT TRAFFIC ASSIGNMENT MODELS

Traffic assignment model	Representative Ref.	Time interval	Real-time congestion, queuing, and EV service
Static	[2], [6], [11]	≥90 min	×
Semi-static	[3]	15-90min	×
Dynamic	[5], [28]	≤15min	√

Due to the inherent short-sightedness of MPC-based methods, several advanced real-time dispatch approaches have emerged in other broader energy system operations. Some research applies linear affine rules to model the relationships between variables, extending MPC's foresight [16], [17]. However, these affine solutions often yield suboptimal results due to linear approximation. Alternatively, other studies split multi-period optimization into single-stage problems connected by cascaded value functions that incorporate future information, thus addressing MPC's limitations and forming a dynamic programming (DP)-formulated multi-stage optimization model [18]. To tackle uncertainties in real-time dispatch, DP-formulated multi-stage SO and RO models have been employed in energy storage systems [19], microgrids [20], and rapid-response devices [21], utilizing stochastic or robust dual dynamic programming (SDDP [18] or RDDP [22]) or their variants [21], [23] to secure high-quality outcomes. Notably, DP-based multi-stage RO sidesteps the complexities introduced by extensive scenario trees in SO counterparts while delivering robust solutions, making it particularly effective for enhancing system resilience and restoration. However, within the context of coordinated PDN and UTN, designing a restoration-oriented traffic-power flow model that incorporates V2G services for real-time interactions between PDN and UTN, and integrating it tractably into a DP-based multi-stage optimization scheme, remains a challenging and unexplored issue.

In summary, existing studies exhibit the following research gaps:

• A gap exists for a post-disaster load restoration model in coordinated PDN and UTN systems that effectively utilizes V2G responses to support critical loads while accommodating the coordinated assignment of V2G-participating EVs with other vehicles. This includes characterizing traffic congestion, queuing, and EV services in UTN within short time intervals.

• There is a lack of an real-time optimization framework for post-disaster load restoration in coordinated PDN and UTN that addresses the short-sightedness of traditional MPC methods, supports rapid computations, and effectively handles uncertainties.

In response, this paper introduces a novel real-time post-disaster load restoration method for coordinated PDN and UTN. The contributions are summarized as follows:

1) A robust load restoration method is proposed that real-time synchronizes distributed resource dispatch in the PDN, network reconfiguration, and congestion-aware V2G responses in the UTN to restore critical loads following a disaster.

2) A practical application framework is developed to support the real-time restoration. The multi-period restoration is offline formulated and tackled as a DP-based multi-stage RO problem to account for uncertainties in DRE generation and O-D traffic demands. Then, a policy-guided decision scheme is featured in real-time restoration, derived from solved value functions that leveraging knowledge of future uncertainties, which addresses the short-sightedness of traditional MPC-based method and can cope with uncertainties effectively.

3) An improved RDDP algorithm is customized for the efficient solution of the DP-based multi-stage RO restoration problem. It employs approximate convex hulls and Lagrange hyperplanes to construct value functions' upper and lower bounds at each stage, refining solutions through iterative forward and backward passes until convergence is achieved.

The rest of this paper is organized as follows. The detailed formulation of proposed post-disaster restoration model is provided in Section II, and Section III presents the practical application framework. Numerical simulation results are reported in Section IV. Section V concludes this study.

II. Mathematical Formulation

A. Problem Descriptions

This study addresses the post-disaster restoration where connections between PDN and substations are disrupted, and certain PDN lines are damaged after a natural disaster. Although society resumes normal operations, some loads remain without power due to damage in the PDN lines. Grid repairs may take hours or days, while vehicles in the UTN resume operations [5], [11], [24]. The proposed V2G-based restoration scheme allows supporting-V2G EVs to assist in load restoration without disrupting their normal O-D tasks. EVs voluntarily assess compensation rewards and travel time costs to decide whether to participate, ensuring both safety and user autonomy.

Fig. 1 outlines the proposed restoration scheme. In the PDN, distributed generators (DGs) and DREs are urgently dispatched, and switches are operated to reconfigure the network into island subsystems to support critical loads. Under V2G coordination, network reconfiguration needs to consider the aggregation of not only DGs and DREs near critical load buses in the PDN, but nearby FCSs for V2G services. Therefore, to enhance load restoration, the optimization for reconfiguration should align with the spatial and temporal status of vehicles within the coordinated PDN and UTN system.

In UTN, varied vehicle travel demands are injected into origin nodes each operation interval, creating multiple O-D tasks. Considering the emergency context, FCSs allocated in UTN nodes are not available for charging services. Vehicles starting from origins per period are classified into EVs with sufficient power that can participate in V2G responses and other vehicles (including EVs unable to support V2G and fuel vehicles). FCSs set compensations to encourage EVs in the UTN for V2G responses, based on the pre-calculated marginal prices [25] of the connected PDN buses, reflecting their power status—whether normal or in shortage. Additionally, congestion and time costs are also considered to ensure the practically viable assignment of V2G EVs and other vehicles in the UTN.

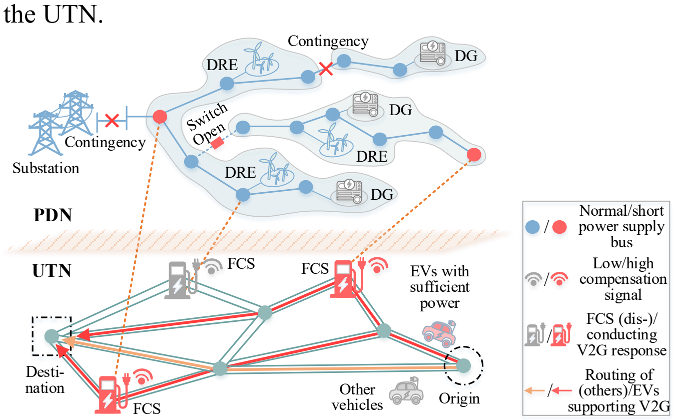

Fig. 1. Illustration of restoration of coordinated PDN and UTN with V2G response

B. Deterministic model formulation

This section presents the basically deterministic formulation for the proposed post-disaster restoration method, excluding uncertainties and the real-time computation framework. The objective function (1) coordinates the operation of the PDN and UTN systems. In the PDN, the objective is to minimize overall load shedding costs, considering the importance ratio of each load to prioritize critical loads, and to maximize the utilization of DRE resources. In the UTN, operation costs, including travel and queue time costs offset by V2G profits, are minimized. The DTA model used captures the evolution of traffic flow over short time segments, where traffic flow and travel time are positively correlated, differing from the Bureau function-based time variable used in STA models. Further details are provided in subsequent descriptions.

$$\begin{aligned}\min \sum_{t\in\mathcal{T}}\{&\sum_{d\in\mathcal{D}} c^{sd}\omega_d Ls_{d,t} + \sum_{w\in\mathcal{W}} c^{ul}[Ar_{w,t}(1+\xi_{w,t}) - Pr_{w,t}] + \\ r^{tv}[&\sum_{k\in\mathcal{K}_b}\sum_{b\in\mathcal{B}}(x^{ge,u}_{b,k,t}+x^{ge,o}_{b,k,t}) + \sum_{k\in\mathcal{K}_h}\sum_{h\in\mathcal{H}^c} x^{qu,u}_{h,k,t}] - \sum_{h\in\mathcal{H}^c}\mu^{cm}_{h,t}Pvg_{h,t}\}\end{aligned} \tag{1}$$

Constraints (2)-(20) based on the linearized DistFlow model [26] ensure power and voltage magnitudes are within permissible ranges during the restoration process. Constraints (2) and (3) limit the active, reactive power, and ramping capabilities of DGs. Constraints (4)-(5) define the consumption and available power characteristics of DERs. Constraints (6)-(13) facilitate PDN reconfiguration into islanded subsystems through switch operations. Specifically, Constraints (6) and (7) ensure a radial topology for the PDN and that each bus belongs to a subsystem. Constraint (8) allows only lines with both ends within the same subsystem to remain active. Constraints (9)-(11), employing the single-commodity flow method [27], guarantee connectivity of PDN subsystems post-reconfiguration: Constraint (9) ensures inflow-outflow balance at each bus using commodity flow, constraint (10) mandates that root buses with DGs send out commodity flow, and constraint (11) verifies that active lines contribute to subsystem connectivity. Constraint (12) indicates power flow changes due to switch operations, with Constraint (13) limiting the total number of switch operations. Voltage regulations through Constraints (14)-(16) fix zero voltage drop at disconnected PDN lines. Constraints (17) and (18) maintain active and reactive power flow balance, while Constraints (19)-(20) enforce network capacity limits.

$$\underline{Pd}_g \le Pd_{g,t} \le \overline{Pd}_g, \underline{Qd}_g \le Qd_{g,t} \le \overline{Qd}_g, \forall g\in\mathcal{G}, \forall t \tag{2}$$

$$R_g^- \le Pd_{g,t} - Pd_{g,t-1} \le R_g^+, \forall g\in\mathcal{G}, \forall t \tag{3}$$

$$0 \le Pr_{w,t} \le Ar_{w,t}(1+\xi_{w,t}), \forall w\in\mathcal{W}, \forall t \tag{4}$$

$$Qr_{w,t} = Pr_{w,t}\cdot tan\,\varphi_w, \forall w\in\mathcal{W}, \forall t \tag{5}$$

$$\sum_{ij\in\mathcal{L}}\sum_{m\in\mathcal{M}} Yl_{ij,m,t} = \sum_{i\in\mathcal{I}}\sum_{m\in\mathcal{M}} Yn_{i,m,t} - \sum_{i\in\mathcal{I}}\phi_i, \forall t \tag{6}$$

$$\sum_{m\in\mathcal{M}} Yn_{i,m,t} = 1, \forall i\in\mathcal{I}, \forall t \tag{7}$$

$$Yl_{ij,m,t} \le Yn_{i,m,t}, Yl_{ij,m,t} \le Yn_{j,m,t}, \forall ij\in\mathcal{L}, \forall m\in\mathcal{M}, \forall t \tag{8}$$

$$\sum_{ij\in\mathcal{L}^{+(i)}} Yf_{ij,t} - \sum_{ij\in\mathcal{L}^{-(i)}} Yf_{ij,t} + Gt_{i,t} = \sum_{m\in\mathcal{M}} Yn_{i,m,t}/|\mathcal{I}|, \forall i\in\mathcal{I}, \forall t \tag{9}$$

$$0 \le Gt_{i,t} \le \phi_i, \forall i\in\mathcal{I}, \forall t \tag{10}$$

$$-\sum_{m\in\mathcal{M}} Yl_{ij,m,t} \le Yf_{ij,t} \le \sum_{m\in\mathcal{M}} Yl_{ij,m,t}, \forall ij\in\mathcal{L}, \forall t \tag{11}$$

$$\sum_{m\in\mathcal{M}} Yl_{ij,m,t} - \sum_{m\in\mathcal{M}} Yl_{ij,m,t-1} = v^{cl}_{ij,t} - v^{op}_{ij,t}, \forall ij\in\mathcal{L}, \forall t \tag{12}$$

$$\sum_{t\in[1:t]}\sum_{ij\in\mathcal{L}}(v^{op}_{ij,t}+v^{cl}_{ij,t}) \le \mathrm{N}^{sp},\ Yl_{ij,m,t}, Yn_{i,m,t}, v^{op}_{ij,t}, v^{cl}_{ij,t} \in\{0,1\}, \forall t \tag{13}$$

$$V_{i,t} = V_{j,t} + (Pf_{ij,t} r_{ij} + Qf_{ij,t} x_{ij}) / V + \partial V_{ij,t}, \forall ij \in \mathcal{L}, \forall t \quad (14)$$

$$-V \sum_{m\in\mathcal{M}} Yl_{ij,m,t} \le \partial V_{ij,t} \le V \sum_{m\in\mathcal{M}} Yl_{ij,m,t}, \forall ij \in \mathcal{L}, \forall t \quad (15)$$

$$\underline{V}_i \sum_{m\in\mathcal{M}} Yn_{i,m,t} \le V_{i,t} \le \overline{V}_i \sum_{m\in\mathcal{M}} Yn_{i,m,t}, \forall i \in \mathcal{I}, \forall t \quad (16)$$

$$\begin{aligned} &\sum_{g\in\mathcal{G}_i} Pd_{g,t} + \sum_{w\in\mathcal{W}_i} Pr_{w,t} + \sum_{h\in\mathcal{H}_i^c} Pvg_{h,t} + \sum_{ij\in\mathcal{L}^{+}(i)} Pf_{ij,t} = \\ &\quad \sum_{ij\in\mathcal{L}^{-}(i)} Pf_{ij,t} + \sum_{d\in\mathcal{D}_i} (LD_{d,t} - Ls_{d,t}),\ Ls_{d,t} \ge 0,\ \forall i \in \mathcal{I}, \forall t \end{aligned} \quad (17)$$

$$\begin{aligned} &\sum_{g\in\mathcal{G}_i} Qd_{g,t} + \sum_{w\in\mathcal{W}_i} Qr_{w,t} + \sum_{h\in\mathcal{H}_i^c} Qvg_{h,t} + \sum_{ij\in\mathcal{L}^{+}(i)} Qf_{ij,t} = \\ &\quad \sum_{ij\in\mathcal{L}^{-}(i)} Qf_{ij,t} + \sum_{d\in\mathcal{D}_i} [QD_{d,t} - (QD_{d,t} / LD_{d,t}) \cdot Ls_{d,t}], \forall i \in \mathcal{I}, \forall t \end{aligned} \quad (18)$$

$$-\overline{Pf}_{ij} \sum_{m\in\mathcal{M}} Yl_{ij,m,t} \le Pf_{ij,t} \le \overline{Pf}_{ij} \sum_{m\in\mathcal{M}} Yl_{ij,m,t}, \forall ij \in \mathcal{L}, \forall t \quad (19)$$

$$-\overline{Qf}_{ij} \sum_{m\in\mathcal{M}} Yl_{ij,m,t} \le Qf_{ij,t} \le \overline{Qf}_{ij} \sum_{m\in\mathcal{M}} Yl_{ij,m,t}, \forall ij \in \mathcal{L}, \forall t \quad (20)$$

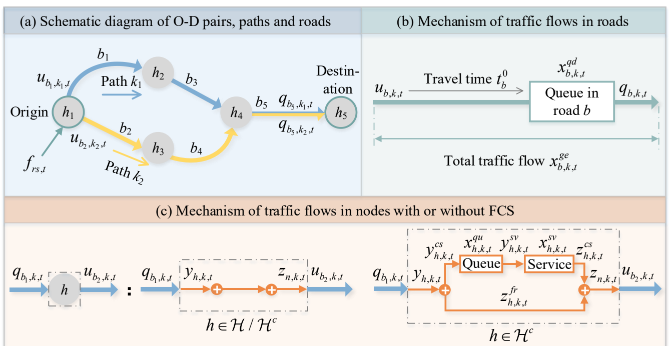

Fig. 2. Schematic of the DTA model

To simulate real-time traffic assignment in UTN, where decision intervals often do not exceed 15 minutes, traditional static [2] or semi-static [3] models used for day-ahead scheduling become unsuitable. This paper employs a DTA model tailored for such short intervals, outlined in constraints (30)-(48) and derived from [28]. In the post-disaster scenario considered in this study, where the goal is to restore critical loads and normalize societal operations, the social optimal criterion is adopted, consistent with approaches used in extreme case scheduling of PDN and UTN [5], [29]. Fig. 2 illustrates the DTA model without differentiating superscripts for EVs supporting V2G (u) and other vehicles (o) for simplicity. Constraint (21) matches the uncertain traffic demands injected into O-D pairs with the inflow at the starting roads of potential routes. For example, b_1 and b_5 denote the start and end roads of route k_1 in Fig. 2(a), respectively. Constraint (22) ensures the total inflow at the starting roads equals the total outflow at the ending roads daily. Indicator parameters $\delta_{b,k}^{r}$ and $\delta_{b,k}^{s}$ identify start and end roads within a route. For instance, if road b is the start of route k, then $\delta_{b,k}^{r} = 1$; otherwise, it is 0. Constraints (23)-(24) describe the dynamic changes in traffic flow on each road, addressing delays and queuing due to limited road capacity, as shown in Fig. 2(b). Finally, constraint (25) establishes the outflow capacity limit.

$$f_{rs,t}^{u/o}(1+\varsigma_{rs,t}^{u/o}) = \sum_{k\in\mathcal{K}_{rs}} \delta_{b,k}^{r} u_{b,k,t}^{u/o}, \forall rs \in \mathcal{O}, \forall b \in \mathcal{B}, \forall t \quad (21)$$

$$\sum_{t\in\mathcal{T}} \delta_{b,k}^{r} u_{b,k,t}^{u/o} = \sum_{t\in\mathcal{T}} \delta_{b,k}^{s} q_{b,k,t}^{u/o}, \forall b \in \mathcal{B}, \forall k \in \mathcal{K}_b, \forall t \quad (22)$$

$$x_{b,k,t}^{qd,u/o} - x_{b,k,t-1}^{qd,u/o} = u_{b,k,t-t_b^0}^{u/o} - q_{b,k,t}^{u/o}, \forall b \in \mathcal{B}, \forall k \in \mathcal{K}_b, \forall t \quad (23)$$

$$x_{b,k,t}^{ge,u/o} - x_{b,k,t-1}^{ge,u/o} = u_{b,k,t}^{u/o} - q_{b,k,t}^{u/o}, \forall b \in \mathcal{B}, \forall k \in \mathcal{K}_b, \forall t \quad (24)$$

$$\sum_{k\in\mathcal{K}_b} (q_{b,k,t}^{u} + q_{b,k,t}^{o}) \le \wp_b, \forall b \in \mathcal{B}, \forall t \quad (25)$$

Fig. 2(c) demonstrates the traffic flow model at normal and FCS nodes within the UTN, where b_1 is the preceding road, and b_2 is the succeeding road of node h. Constraints (26)-(27) establish that the inflow at each node matches the outflow from its preceding road, and the outflow aligns with the inflow from its succeeding road. Parameters $\sigma_{b,h,k}^{pr}$ and $\sigma_{b,h,k}^{su}$ determine whether road b is a predecessor or successor to node h in route k. If road b is the predecessor of node h, then $\sigma_{b,h,k}^{pr} = 1$; otherwise, it is 0. Constraint (28)-(29) ensures that the inflow and outflow of EVs supporting V2G at normal nodes, as well as other vehicles at both FCS and regular nodes, are balanced. Constraint (30) specifies that the inflow of EVs supporting V2G at FCS nodes includes both V2G response and non-response flows, while constraint (31) similarly defines the outflow. Constraint (32) guarantees the balance of total inflow and outflow for EVs participating in V2G responses. Constraints (33)-(34) account for dynamic queue and services in V2G flows within FCS nodes, considering the limited capacity of the FCSs. Constraint (35) sets the FCS capacities for V2G responses. Constraint (36) limits the V2G response flow for each route, ensuring it does not exceed the total number of injected V2G-supported EVs minus those that have already completed a V2G response. Constraint (37) permits EVs with sufficient power to opt in or out of V2G activities, while ensuring the number of participants does not exceed the totally injected limit. Constraints (38) specify that the power returned to the PDN by FCSs in each period is proportional to the current V2G flow. Finally, Constraint (39) defines the reactive power characteristics of FCSs.

$$q_{b,k,t}^{u/o} = \sigma_{b,h,k}^{pr} y_{h,k,t}^{u/o}, \forall b \in \mathcal{B}, \forall h \in \mathcal{H}, \forall k \in \mathcal{K}_b \cap \mathcal{K}_h, \forall t \quad (26)$$

$$u_{b,k,t}^{u/o} = \sigma_{b,h,k}^{su} z_{h,k,t}^{u/o}, \forall b \in \mathcal{B}, \forall h \in \mathcal{H} / \mathcal{H}^c, \forall k \in \mathcal{K}_b \cap \mathcal{K}_h, \forall t \quad (27)$$

$$y_{h,k,t}^{o} = z_{h,k,t}^{o}, \forall h \in \mathcal{H}, \forall k \in \mathcal{K}_h, \forall t \quad (28)$$

$$y_{h,k,t}^{u} = z_{h,k,t}^{u}, \forall h \in \mathcal{H} / \mathcal{H}^c, \forall k \in \mathcal{K}_h, \forall t \quad (29)$$

$$y_{h,k,t}^{u} = y_{h,k,t}^{cs,u} + z_{h,k,t}^{fr,u}, \forall h \in \mathcal{H}^c, \forall k \in \mathcal{K}_h, \forall t \quad (30)$$

$$z_{h,k,t}^{u} = z_{h,k,t}^{cs,u} + z_{h,k,t}^{fr,u}, \forall h \in \mathcal{H}^c, \forall k \in \mathcal{K}_h, \forall t \quad (31)$$

$$\sum_{t\in\mathcal{T}} y_{h,k,t}^{cs,u} = \sum_{t\in\mathcal{T}} z_{h,k,t}^{cs,u}, \forall h \in \mathcal{H}^c, \forall k \in \mathcal{K}_h, \forall t \quad (32)$$

$$x_{h,k,t}^{qu,u} - x_{h,k,t-1}^{qu,u} = y_{h,k,t}^{cs,u} - y_{h,k,t}^{sv,u}, \forall h \in \mathcal{H}^c, \forall k \in \mathcal{K}_h, \forall t \quad (33)$$

$$x_{h,k,t}^{sv,u} - x_{h,k,t-1}^{sv,u} = y_{h,k,t}^{sv,u} - z_{h,k,t}^{cs,u}, \forall h \in \mathcal{H}^c, \forall k \in \mathcal{K}_h, \forall t \quad (34)$$

$$\sum_{k\in\mathcal{K}_h} x_{h,k,t}^{sv,u} \le \Gamma_h, \forall h \in \mathcal{H}^c, \forall t \quad (35)$$

$$\sum_{h\in\mathcal{H}^c} y_{h,k,t}^{cs,u} \le \sum_{t\in[1:t]} \delta_{b,k}^{r} u_{b,k,t}^{u} - \sum_{t\in[1:t]} \sum_{h\in\mathcal{H}^c} z_{h,k,t}^{cs,u}, \forall k \in \mathcal{K}, \forall t \quad (36)$$

$$\sum_{t\in\mathcal{T}} \sum_{k\in\mathcal{K}_{rs}\cap\mathcal{K}_h} \sum_{n\in\mathcal{H}^c} z_{h,k,t}^{cs,u} \le \sum_{t\in\mathcal{T}} [f_{rs,t}^{u}(1+\varsigma_{rs,t}^{u})], \forall rs \in \mathcal{O} \quad (37)$$

$$Pvg_{h,t} = \sum_{k\in\mathcal{K}_h} x_{h,k,t}^{sv,u} \cdot \Delta p, \forall n \in \mathcal{H}^c, \forall t \quad (38)$$

$$Qev_{h,t} = Pvg_{h,t} \cdot tan\,\varphi_h, \forall h \in \mathcal{H}^c, \forall t \tag{39}$$

It is worth mentioning that Refs. [30] and [31] propose DTA under user equilibrium to model UTN operation, reformulating the model using variational inequality and an iterative method to handle non-linearity. Ref. [5] considers extreme conditions, similar to this study, with a social optimality-based DTA formulation. Due to the complexity of time-dependent travel variables, the model is also nonlinear, requiring an iterative framework with alternating updates and fixed flow propagation variables, like in [30] and [31]. The DTA model employed in this study maps time-varying travel times to output EV flows (Fig. 2(b)), discretizing nonlinear flow constraints and transforming the model into a linear optimization problem. This makes it easier to integrate into uncertainty-aware scheduling models.

C. Uncertainties characterization

The DRE output and O-D traffic demands are considered as uncertain variables in this study, as shown in (40). To capture these uncertainties, we introduce a data-driven polyhedral uncertainty set based on PCA [32], focusing on relative prediction errors. $\boldsymbol{\mu}_t^{re}$ and $\boldsymbol{\mu}_t^{ta}$ represent the mean matrices, and $\boldsymbol{D}_t^{re}$ and $\boldsymbol{D}_t^{ta}$ are the covariance matrices for DRE output and traffic demands at period t, derived via PCA. The normalized uncertain parameter is denoted by $\boldsymbol{\theta}_t^{re(ta)}$, and adjustable factors $\Pi_1^{re(ta)}$ and $\Pi_2^{re(ta)}$ balance cost-effectiveness and robustness.

$$\boldsymbol{\xi}_t = \{\xi_{w,t} \mid w \in \mathcal{W}\},\ \boldsymbol{\varsigma}_t = \{\varsigma_{rs,t}^{u/o} \mid rs \in \mathcal{O}\}, \forall t \tag{40}$$

$$\Xi_t = \left\{ \boldsymbol{\xi}_t \left| \begin{array}{l} \boldsymbol{\xi}_t = \boldsymbol{\mu}_t^{re} + \boldsymbol{D}_t^{re}\boldsymbol{\theta}_t^{re} \\ \left\|\boldsymbol{\theta}_t^{re}\right\|_1 \le \Pi_1^{re} \\ \left\|\boldsymbol{\theta}_t^{re}\right\|_\infty \le \Pi_2^{re} \end{array} \right. \right\} \cup \left\{ \boldsymbol{\varsigma}_t \left| \begin{array}{l} \boldsymbol{\varsigma}_t = \boldsymbol{\mu}_t^{ta} + \boldsymbol{D}_t^{ta}\boldsymbol{\theta}_t^{ta} \\ \left\|\boldsymbol{\theta}_t^{ta}\right\|_1 \le \Pi_1^{ta} \\ \left\|\boldsymbol{\theta}_t^{ta}\right\|_\infty \le \Pi_2^{ta} \end{array} \right. \right\}, \forall t \tag{41}$$

The proposed data-driven uncertainty set reduces the conservatism inherent in the traditional box uncertainty set used in the RO method [21]. This is achieved in two ways: 1. It uses historical data to determine the center of the uncertainty set, and 2. It adopts a polyhedral form, which effectively eliminates regions with extremely low probabilities compared to the box form. Additionally, to further reduce conservatism, the values of parameters $\Pi_1^{re(ta)}$ and $\Pi_2^{re(ta)}$ can be adjusted.

D. Reformulation to DP-based multi-stage RO model

To enable real-time application, we reformulate the above deterministic model into a DP-based multi-stage RO model. Firstly, a multi-stage RO problem (42) is set up to integrate the proposed restoration approach and uncertainty set, where the nested "max-min" operators are used to make resilient decisions that can withstand the worst-case scenario, ensuring feasibility across all scenarios under post-disaster conditions.

$$\begin{aligned} & \min_{\boldsymbol{p}_1}[\boldsymbol{c}_1^\top \boldsymbol{p}_1 + \max_{\xi_2,\varsigma_2 \in \Xi_2} \min_{\boldsymbol{p}_2}(\boldsymbol{c}_2^\top \boldsymbol{p}_2 + \cdots \max_{\xi_T,\varsigma_T \in \Xi_T} \min_{\boldsymbol{p}_T} \boldsymbol{c}_T^\top \boldsymbol{p}_T)] \\ & s.t.\ \boldsymbol{D}_1 \boldsymbol{p}_1 \le \boldsymbol{h}_1 \\ & \quad \boldsymbol{E}_t \boldsymbol{p}_{t-1} + \boldsymbol{D}_t \boldsymbol{p}_t(\boldsymbol{\xi}_t, \boldsymbol{\varsigma}_t) \le \boldsymbol{h}_t(\boldsymbol{\xi}_t, \boldsymbol{\varsigma}_t) \quad \forall t = 2,...,T \\ & \quad \boldsymbol{p}_t(\boldsymbol{\xi}_t, \boldsymbol{\varsigma}_t) \in \mathbb{R}^n \cup \mathbb{B}^m, \forall t \end{aligned} \tag{42}$$

where, $\boldsymbol{p}_t$ denotes the dispatch variables for the PDN and UTN systems in period t. The vector $\boldsymbol{p}_{t\text{-}1}$ covers the decisions made in the preceding periods [1:t–1]. The cost coefficients for real-time decisions in period t are denoted by $\boldsymbol{c}_t$. Each period's decision $\boldsymbol{p}_t$ is dependent only on the uncertainty realizations $\boldsymbol{\xi}_t$, $\boldsymbol{\varsigma}_t$ for that period, adhering to stage-wise independence. $\boldsymbol{D}_t$ represents the coefficient matrices for the constraints (2)-(39). $\boldsymbol{E}_t$ links dynamic constraints, such as DGs ramping (3) and dynamic traffic flow evolution (23)-(24), across stages. $\boldsymbol{h}_t$ is a right-hand side function matrix that varies with $\boldsymbol{\xi}_t$ and $\boldsymbol{\varsigma}_t$.

Then, the problem (42) is transformed into Bellman's DP formulation, as detailed in (43)-(45), where the T-period restoration is recast as T-stage problems Q_t ($t\in[1,T]$) linked through cascaded value functions $\mathcal{Q}_{t+1}$ ($t\in[1,T\text{-}1]$). The DP-based multi-stage RO model is leaded by follows:

$$\begin{aligned} Q_1 = \min\ & \boldsymbol{c}_1^\top \boldsymbol{p}_1 + \mathcal{Q}_2(\boldsymbol{p}_1) \\ s.t.\ & \boldsymbol{D}_1 \boldsymbol{p}_1 \le \boldsymbol{h}_1 \\ & \boldsymbol{p}_1 \in \mathbb{R}^n \cup \mathbb{B}^m \end{aligned} \tag{43}$$

The value function $\mathcal{Q}_{t+1}(\boldsymbol{p}_t)$ quantifies the total future cost associated with decision $\boldsymbol{p}_t$ under the worst-case uncertainties realization for the restoration of coupled PDN and UTN. It is calculated as:

$$\mathcal{Q}_{t+1}(\boldsymbol{p}_t) = \max\{Q_{t+1}(\boldsymbol{p}_t; \boldsymbol{\xi}_{t+1}, \boldsymbol{\varsigma}_{t+1}) : \boldsymbol{\xi}_{t+1}, \boldsymbol{\varsigma}_{t+1} \in \Xi_{t+1}\} \tag{44}$$

where, t-th stage problem $Q_t(\boldsymbol{p}_{t\text{-}1}; \boldsymbol{\xi}_t, \boldsymbol{\varsigma}_t)$ is defined as:

$$\begin{aligned} Q_t(\boldsymbol{p}_{t-1}; \boldsymbol{\xi}_t, \boldsymbol{\varsigma}_t) = \min\ & \boldsymbol{c}_t^\top \boldsymbol{p}_t + \mathcal{Q}_{t+1}(\boldsymbol{p}_t) \\ s.t.\ & \boldsymbol{E}_t \boldsymbol{p}_{t-1} + \boldsymbol{D}_t \boldsymbol{p}_t \le \boldsymbol{h}_t(\boldsymbol{\xi}_t, \boldsymbol{\varsigma}_t) \\ & \boldsymbol{p}_t \in \mathbb{R}^n \cup \mathbb{B}^m, \forall t \end{aligned} \tag{45}$$

III. Proposed Solution Method and Application Framework

In the proposed application framework, the DP-based multi-stage RO model is solved by a proposed improved RDDP algorithm to derive optimal decision policies. Then, the real-time restoration decisions are swiftly made through the solution of T policy-guided single-period problems.

A. Offline optimization

The offline optimization focuses on formulating and solving the model proposed in Section II. This type of DP-based multi-stage RO model can be tackled using either the traditional [22] or enhanced RDDP algorithms [19], both of which require the value function $\mathcal{Q}_{t+1}(\boldsymbol{p}_t)$ to be convexity. However, the presence of both binary and continuous elements in the state variable $\boldsymbol{p}_t$ introduces non-convexity. To address this issue, we employ a smoothing technique inspired by SDDiP [23], which binarizes all state variables, thereby converting $\boldsymbol{p}_t$ into a binarized form $\boldsymbol{p}_t^\nabla$ using a piecewise approach. This allows the non-convex $\mathcal{Q}_{t+1}(\boldsymbol{p}_t)$ to be transformed into $\mathcal{Q}_{t+1}(\boldsymbol{p}_t^\nabla)$ with a convex lower envelope. Following this, an improved RDDP algorithm is developed that establishes two bounds for the value functions as $\underline{\mathcal{Q}}_{t+1}(\boldsymbol{p}_t^\nabla) \le \mathcal{Q}_{t+1}(\boldsymbol{p}_t^\nabla) \le \overline{\mathcal{Q}}_{t+1}(\boldsymbol{p}_t^\nabla)$. This approach decomposes the DP problem into T upper and lower approximation subproblems (denoted by (46) and (47)), which are iteratively refined to close the gap between the bounds and the actual value function until convergence is achieved.

$$\begin{aligned} \overline{Q}_t(\boldsymbol{p}_{t-1}^\nabla) = \max_{\xi_t,\varsigma_t \in \Xi_t} \min\ & \boldsymbol{c}_t^\top \boldsymbol{p}_t^\nabla + \overline{\mathcal{Q}}_{t+1}(\boldsymbol{p}_t^\nabla) \\ s.t.\ & \boldsymbol{E}_t \boldsymbol{p}_{t-1}^\nabla + \boldsymbol{D}_t \boldsymbol{p}_t^\nabla \le \boldsymbol{h}_t(\boldsymbol{\xi}_t, \boldsymbol{\varsigma}_t) \\ & \boldsymbol{p}_t^\nabla \in \mathbb{B}^{n+m}, \forall t \end{aligned} \tag{46}$$

$$\begin{aligned}\underline{Q}_t(\boldsymbol{p}_{t-1}^{\nabla};\boldsymbol{\xi}_t,\boldsymbol{\varsigma}_t)=\min\ & \boldsymbol{c}_t^{\top}\boldsymbol{p}_t^{\nabla}+\underline{Q}_{t+1}(\boldsymbol{p}_t^{\nabla})\\ s.t.\ & \boldsymbol{E}_t\boldsymbol{p}_{t-1}^{\nabla}+\boldsymbol{D}_t\boldsymbol{p}_t^{\nabla}\le\boldsymbol{h}_t(\boldsymbol{\xi}_t,\boldsymbol{\varsigma}_t)\\ & \boldsymbol{p}_t^{\nabla}\in\mathbb{B}^{n+m},\forall t\end{aligned}\tag{47}$$

For the lower approximation of $\underline{Q}_{t+1}(\boldsymbol{p}_{t-1}^{\nabla})$, the hyperplane method is utilized. Traditional Benders hyperplanes are ineffective for the multi-stage RO model due to the inapplicability of the strong dual theorem with discrete variables. To address this, the improved RDDP algorithm employs Lagrangian hyperplanes, as in SDDiP [23], to establish a tight lower bound for DP-based multi-stage models with mixed-integer recourse variables, using the zero-gap Lagrangian dual theorem. These Lagrangian hyperplanes are constructed by solving a relaxation problem for $\underline{Q}_t$ based on uncertainty realizations (ξ_t, ς_t) from the upper approximation problem (48).

$$\begin{aligned}\mathfrak{L}[\underline{Q}_t(\boldsymbol{p}_{t-1}^{\nabla};\boldsymbol{\xi}_t,\boldsymbol{\varsigma}_t)]=\max_{\boldsymbol{\pi}_t}\ & \boldsymbol{\pi}_t^{\top}\boldsymbol{p}_{t-1}^{\nabla}+\boldsymbol{\Phi}_t\\ where:\ \boldsymbol{\Phi}_t=\min_{\boldsymbol{p}_t^{\nabla},\boldsymbol{\upsilon}_t}\ & \boldsymbol{c}_t^{\top}\boldsymbol{p}_t^{\nabla}+\underline{Q}_{t+1}(\boldsymbol{p}_t^{\nabla})+\boldsymbol{\eta}_t\\ s.t.\ & \boldsymbol{\eta}_t\ge-\boldsymbol{\pi}_t^{\top}\boldsymbol{\upsilon}_t,\ \ \boldsymbol{\upsilon}_t=\boldsymbol{p}_{t-1}^{\nabla}\\ & \boldsymbol{E}_t\boldsymbol{p}_{t-1}^{\nabla}+\boldsymbol{D}_t\boldsymbol{p}_t^{\nabla}\le\boldsymbol{h}_t(\boldsymbol{\xi}_t,\boldsymbol{\varsigma}_t)\\ & \boldsymbol{p}_t^{\nabla}\in\mathbb{B}^{n+m},\boldsymbol{\upsilon}\in\mathbb{R}^{n+m}\end{aligned}\tag{48}$$

Through the solution of (48), the coefficient of the Lagrangian hyperplanes, denoted as $\boldsymbol{\pi}_t^*$, along with the objective value $\boldsymbol{\Phi}_t^*$, can be determined. The Lagrangian hyperplanes are then added into refine $\underline{Q}_{t+1}(\boldsymbol{p}_t^{\nabla})$ in problem (48) and are expressed as $\underline{Q}_{t+1}(\boldsymbol{p}_t^{\nabla})\ge\boldsymbol{\Phi}_{t+1}^*+\boldsymbol{\pi}_{t+1}^{*\top}\boldsymbol{p}_t^{\nabla}$.

In the upper approximation problem (46), the upper bound $\overline{Q}_{t+1}(\boldsymbol{p}_t^{\nabla})$ is obtained using a convex hull-based method. The conventional RDDP algorithm constructs the convex hull by enumerating extreme points [22], but this process is computationally demanding. To improve efficiency, this study introduces an approximate convex hull construction technique that employs convex combinations of sample points and penalty boundaries. The detailed formulation is provided as follows:

$$\begin{aligned}\overline{Q}_t(\boldsymbol{p}_{t-1}^{\nabla})=\max_{\boldsymbol{\xi}_t,\boldsymbol{\varsigma}_t\in\Xi_t}\min\ & \boldsymbol{c}_t^{\top}\boldsymbol{p}_t^{\nabla}+\underbrace{\sum_{s\in S_t}\Theta_t^{s}\lambda_s+\boldsymbol{\alpha}_t^{k}(\boldsymbol{\Delta}_t^{+}+\boldsymbol{\Delta}_t^{-})}_{\overline{Q}_{t+1}(\boldsymbol{p}_t^{\nabla})}\\ s.t.\ & \boldsymbol{E}_t\boldsymbol{p}_{t-1}^{\nabla}+\boldsymbol{D}_t\boldsymbol{p}_t^{\nabla}\le\boldsymbol{h}_t(\boldsymbol{\xi}_t,\boldsymbol{\varsigma}_t)\\ & \sum_{s\in S_t}\lambda_s=1,\ \lambda_s\ge0,\ \forall s\in S_t\\ & \sum_{s\in S_t}\lambda_s\boldsymbol{p}_t^{\nabla s}+\boldsymbol{\Delta}_t^{+}-\boldsymbol{\Delta}_t^{-}=\boldsymbol{p}_t^{\nabla},\ \boldsymbol{\Delta}_t^{+}\ge0,\ \boldsymbol{\Delta}_t^{-}\ge0\\ & \boldsymbol{\Delta}_t^{+},\boldsymbol{\Delta}_t^{-}\in\mathbb{R}^{n+m},\boldsymbol{p}_t^{\nabla}\in\mathbb{B}^{n+m},\lambda_s\in\mathbb{R}^{1}\end{aligned}\tag{49}$$

In equation (49), the candidate state variable $\boldsymbol{p}_t^{\nabla}$ for $\overline{Q}_{t+1}(\boldsymbol{p}_t^{\nabla})$ is classified as either inside or outside the convex hull. If $\boldsymbol{p}_t^{\nabla}$ falls within the range of previous sample points, $\overline{Q}_{t+1}(\boldsymbol{p}_t^{\nabla})$ is expressed as a convex combination of these past points, denoted by ($\boldsymbol{p}_t^{\nabla s}$, Θ_t^s), using coefficients λ_s. For decisions outside this range, penalties are applied via boundary lines with adaptive penalty slopes $\boldsymbol{\alpha}_t^k$ [19], whose formulation is shown in (50). To handle the bilevel problem (49), vertex enumeration for Ξ_t is adopted. The iterative construction of the convex hull $\overline{Q}_{t+1}(\boldsymbol{p}_t^{\nabla})$ is shown in Fig. 3.

$$\boldsymbol{\alpha}_t^k=\rho\cdot\max\{\boldsymbol{\pi}_t^{*(j)},\ \forall j\in1:k(k\ge2)\}\tag{50}$$

where $\boldsymbol{\pi}_t^{*(j)}$ represents historical values from iterations 1 to k. The parameter ρ, tested to be between 1.5 and 2.0, ensures RIA remains above $\mathcal{Q}_{t+1}(\boldsymbol{p}_t^{\nabla})$. With thes adaptive $\boldsymbol{\alpha}_t^k$, the convex hull can explore more sample points at the beginning of the improved RDDP iteration, accelerating convergence and ensuring the optimality of solutions by the end of the iteration.

The use of the approximate convex hull method for upper approximation has been effective in multi-stage RO problems with continuous recourse variables [19], [33], though its application to binary-transformed nonconvex value functions have not been investigated. However, Fig. 3 demonstrates that the improved RDDP algorithm remains effective in this context. The convex lower envelope aligns with the value functions at all decision sample points [23], and the upper approximation of binary-transformed value functions can match the lower envelope. Additionally, the approximate convex hull technique has been proven to provide tight and finite upper approximations for convex value functions [33]. Thus, despite the nonconvex nature of binary-transformed value functions, the improved RDDP algorithm is guaranteed to converge finitely, due to the effectiveness of both Lagrangian hyperplanes and the convex hull approach.

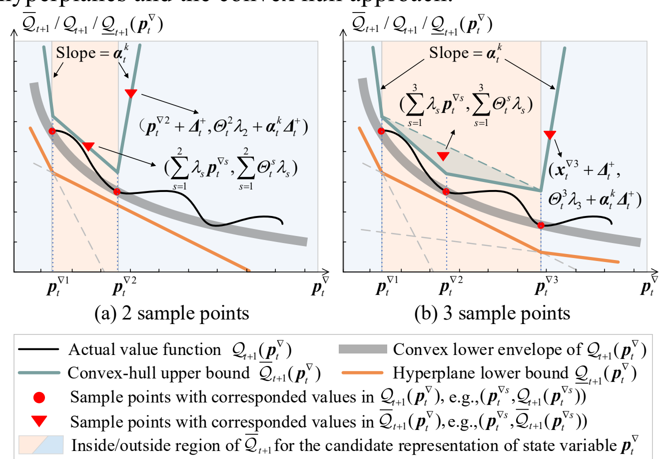

Fig. 3. Iterative and effectiveness demonstration of improved RDDP algorithm

The overall execution of the developed improved RDDP algorithm will be presented in Fig. 4(b), which is divided into *Forward pass* and *Backward pass* produces. During the *Forward pass*, which progresses from $t\in[1:T]$, the worst-case uncertainties realization (ξ_t, ς_t) is identified by solving the problem $\overline{Q}_t(\boldsymbol{p}_{t-1}^{\nabla})$, and decision samples $\boldsymbol{p}_t^{\nabla}$ are generated by solving the problem $\underline{Q}_t(\boldsymbol{p}_{t-1}^{\nabla};\boldsymbol{\xi}_t,\boldsymbol{\varsigma}_t)$. In the *Backward pass*, which proceeds from $t\in[T:1]$, effective sample points are incorporated to refine the upper bound in (49), and inequalities are formulated to update the lower bound as (48).

B. Real-time restoration

To facilitate real-time post-disaster restoration of coordinated PDN and UTN systems, a policy-guided decision scheme is introduced, according to the real-time measurements of DRE outputs and traffic demands. Specifically, by solving the proposed DP-based multi-stage RO model in the offline optimization, the solved value functions $\mathcal{Q}_{t+1}^*$ for each dispatch period ($t\in[1,T-1]$) are obtained by filtering out the final $\underline{Q}_{t+1}$

after the RDDP algorithm terminates. Aggregating future information into hyperplanes formulated policies, real-time distributed resource generation, network reconfiguration, and V2G responses can be swiftly directed. The policy-guided restoration problem (51) for period t follows the same formulation as Q_t. While the dispatch policy $\mathcal{Q}_{t+1}^*$, along with the real-time measured DRE power ξ_t^* and traffic demand ς_t^*, are input as parameters.

$$\begin{aligned} &\min\ \boldsymbol{c}_t^\top \boldsymbol{p}_t^\nabla + \mathcal{Q}_{t+1}^*(\boldsymbol{p}_t^\nabla) \\ &s.t.\ \boldsymbol{E}_t \boldsymbol{p}_t^\nabla + \boldsymbol{D}_t \boldsymbol{p}_t^\nabla \le \boldsymbol{h}_t(\xi_t^*, \varsigma_t^*) \end{aligned} \tag{51}$$

Since $\mathcal{Q}_{t+1}^*$ encapsulates aggregated future information, including both decision relationships and uncertainties, only T single-period problems need to be solved during the real-time restoration of the coupled PDN and UTN system. This proposed real-time restoration method effectively accounts for uncertainties with robustness and overcomes the short-sightedness of MPC and affine rule-based methods. Additionally, it improves computational efficiency by eliminating the need for additional rolling horizons.

C. Overall process of application framework

The flowchart of the proposed application framework for real-time restoration of coordinated PDN and UTN systems is summarized in Fig. 4. In the offline optimization, the process starts with data initialization, identifying the post-disaster system state, and collecting predicted DRE output and traffic demand. We pre-solve a deterministic optimal dispatch model considering only the PDN and extract the marginal prices (dual multipliers) as input for the restoration method. This provides more accurate electricity price parameters than studies [28], [34], which set prices artificially. Notably, other advanced dynamic marginal pricing schemes that account for the PDN-UTN interaction [25], [30] can also be directly integrated into the compensation price acquisition step in the offline portion of Fig. 4. The DP-based multi-stage RO model is then formulated and solved using the improved RDDP algorithm to derive real-time policies $\mathcal{Q}_{t+1}^*$.

In the real-time application, T-period decoupled restoration problems are solved sequentially. For each period t, the measured DRE power and traffic demand are input into the policy-guided restoration problem (51), quickly determining binarized restoration decisions $\boldsymbol{p}_t^\nabla$. The reverse binarization method [35] is then applied to convert the binary decision $\boldsymbol{p}_t^\nabla$ back to its continuous counterpart.

IV. Case Study

A. Simulation setting

The effectiveness of the proposed real-time restoration method is demonstrated using a modified IEEE 33-bus PDN with a 20-road UTN (33P-20U) and a real-world system in Zhejiang Province, China, comprising 91 PDN buses and 35 UTN roads. It is worth mentioning that the UTN considered in this study spans one or more districts within a medium-sized city, with the longest road measuring around 50 km [36]. Travel on each road, assuming no congestion, can be completed within an hour, ensuring high user participation in V2G without altering their destination. The load shedding penalty is set at

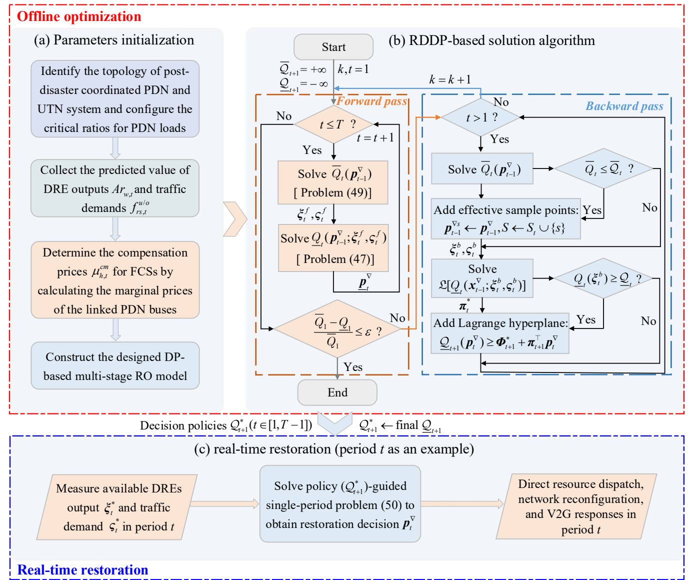

Fig. 4. Flowchart demonstration of proposed application framework

\$40/kWh, while the DRE curtailment cost is \$8/kWh. The queue cost coefficient for UTN nodes and roads is \$0.2 per vehicle per period, and the total operations for soft open switches is capped at 12. Uncertainty factors Π_1 and Π_2 are set to 2 and 1.5. V2G service prices at each FCS are based on the marginal price of the corresponding PDN bus, calculated from the dual multiplier after solving the restoration model without uncertainties. The convergence criterion for the improved RDDP algorithm is set to $\varepsilon = 0.001$, with network parameters, load critical ratios, and UTN information integrated into [37]. To evaluate the proposed real-time restoration method, three comparative techniques are introduced for benchmarking:

- Case I: MPC-based real-time restoration method that does not account for uncertainties [12].
- Case II: Affine multi-stage RO formulated offline optimization, solved with linear and binary rules; real-time restoration guided by affine policies [17].
- Case III: DP-based multi-stage SO formulated offline optimization, solved via SDDiP; real-time restoration guided by expected solved value functions [20].
- Case IV: Proposed DP-based multi-stage RO for offline optimization, solved with the improved RDDP algorithm; real-time restoration guided by worst-case solved value functions.

This section presents both in-sample and out-of-sample tests. The in-sample test monitors restoration decisions across all periods for the coordinated PDN and UTN, filtering uncertainties through offline solutions. The out-of-sample test employs the Monte Carlo (MC) method to simulate real-time restoration performance across various scenarios, assessing the effectiveness of Cases I-IV.

B. Results of 33P-20U system

The topology of the 33P-20U system is depicted in Fig. 5, showing each FCS at a UTN node connected to a PDN bus, with disaster-affected power lines highlighted. After 836.158 seconds of calculations using the improved RDDP algorithm, the offline optimization generates solved value functions for real-time restoration policies. The effectiveness of the proposed DP-based multi-stage RO model is evaluated by tracking in-sample restoration decisions and realized uncertainties, as presented in Fig. 6.

In Fig. 6(a), during low total load demand periods (e.g., periods 1-32), the system prioritizes DRE and V2G responses to enhance renewable consumption and secure subsidies, while DG is flexibly adjusted to maintain power balance. As demand rises (after period 33), DG operates at full capacity, with DRE and V2G maximally dispatched to restore critical loads, showcasing the scheme's flexibility in resource allocation for sustainability and social optimality. Figs. 6(b)-(d) reveal that DRE output often remains at the lower bound of the uncertainty interval, leading to insufficient power generation and load shedding. When the uncertainty interval widens and resources are ample (initial periods of Figs. 6(b) and 6(d)), DRE output fluctuates, resulting in renewable energy curtailment penalties due to inadequate DG ramping capacity. Figs. 6(e)-(f) illustrate traffic demand uncertainty in the UTN, where non-V2G-supporting vehicles consistently hit the upper boundary of the uncertainty interval, exacerbating congestion. Sufficient PDN resources push V2G EVs to the upper boundary, increasing system congestion (e.g., periods 2-31), while resource shortages drop EVs to the lower boundary, causing more load shedding (periods 31-66 and 75-96). During peak evening hours, the substantial number of V2G EVs collaborates with DRE to address critical loads, reaching the upper boundary and triggering DRE curtailment penalties. Overall, the value functions embedded in the proposed DP-based multi-stage RO model effectively accommodate extreme scenarios, yielding resilient real-time restoration policies.

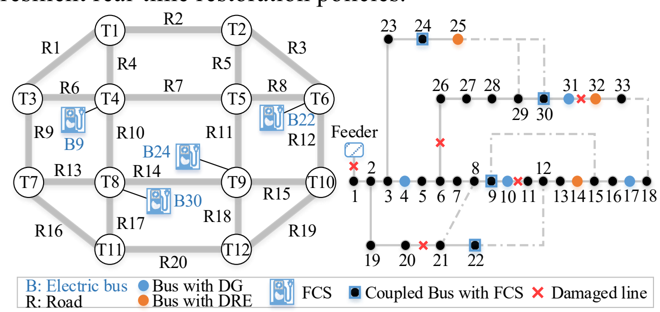

Fig. 5. Topology of 33P-20U system with contingencies

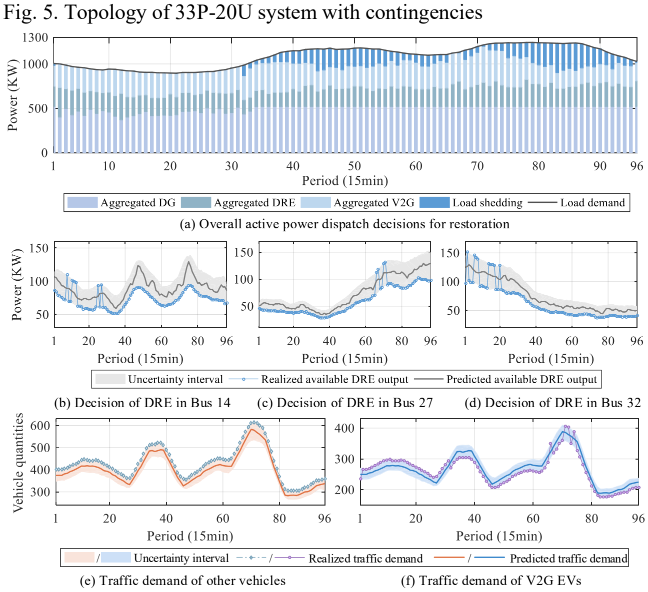

(a) Overall active power dispatch decisions for restoration

(b) Decision of DRE in Bus 14 (c) Decision of DRE in Bus 27 (d) Decision of DRE in Bus 32

(e) Traffic demand of other vehicles (f) Traffic demand of V2G EVs

Fig. 6. In-sample restoration decisions and uncertainties realization

The in-sample network reconfiguration decisions are shown in Fig. 7. During the initial operational period, the system is divided into multiple isolated subsystems based on the post-disaster topology. When total load demand is low (Fig. 7(a)), each subsystem utilizes DRE or V2G responses at FCSs to serve a wide range of load buses, enhancing renewable energy consumption and social benefits. However, when load demand exceeds resource capacity, the topology adjusts to accommodate more critical loads. In Fig. 7(b), the DG at Bus 4 cannot support an independent subsystem, prompting the reclassification of DRE at Bus 25 and FCS at Bus 24 for critical load restoration. Additionally, the FCS at Bus 30, which has the highest V2G response after period 33, is reconfigured to work with the DG at Bus 31, demonstrating the flexibility and robustness of the proposed scheme.

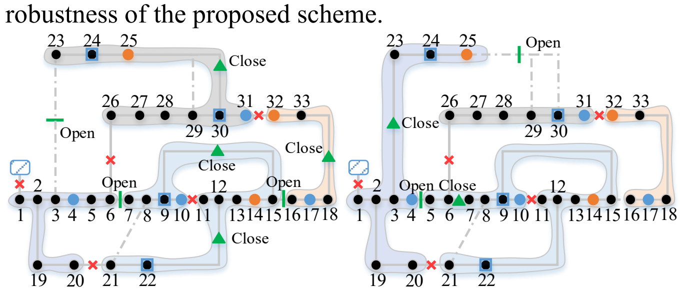

(a) Network reconfiguration in period 1 (b) Network reconfiguration in period 33

Fig. 7. Network reconfiguration decisions during restoration process

To monitor the V2G responses in the UTN, Fig. 8 illustrates the number of EVs conducting V2G services and the corresponding compensation prices at each FCS. The figure shows that EVs generally respond to the FCS at node 9, where higher compensation prices are offered. Meanwhile, node 8 also sees a large number of V2G EVs due to its high capacity and central location along multiple routes. This V2G response assignment effectively balances economic benefits, traveling costs, and equipment parameters.

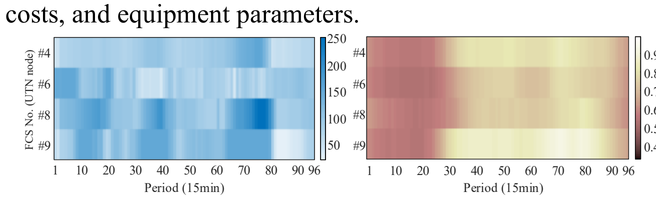

(a) Quantities of EVs conducting V2G services (b) Marginal price based compensation price ($/KWh)

Fig. 8. Quantities of V2G EVs and compensation prices of each FCS

To further validate the DTA model, Fig. 9 illustrates the in-sample dynamic node and V2G traffic flow for period 70, while Fig. 10 presents inflow, queuing, outflow, and service flows for representative UTN nodes and roads across all periods. Unlike the STA model, the DTA model dynamically tracks EV flows—entering, queuing, and exiting roads and FCS nodes—providing granular insights in short time intervals, particularly for real-time assignment. The inflow-outflow constraints between roads and nodes are consistently satisfied. In Fig.10(a), morning peak and road capacity limitations lead to increased queue flow, with outflow kept at the upper limit to clear congestion until the evening peak ends, minimizing travel costs in the UTN. Fig. 10(b) shows a similar relationship among node inflow, outflow, and queuing. DTA delay (t_b^0) creates a temporary mismatch between inflow and outflow, enhancing traffic assignment flexibility. For example, in Fig. 10(b), node outflow is increased in advance to alleviate congestion and free

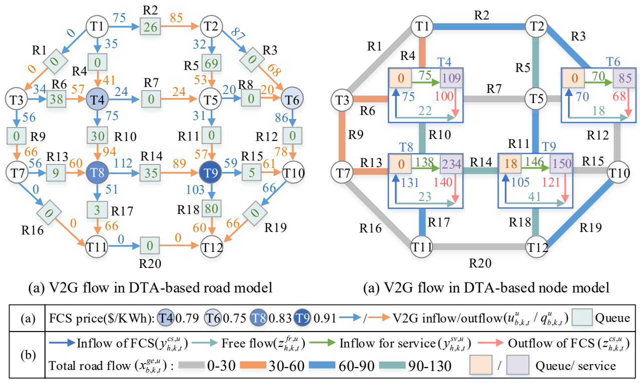

Fig. 9. DTA-based road and node V2G flows in typical restoration period

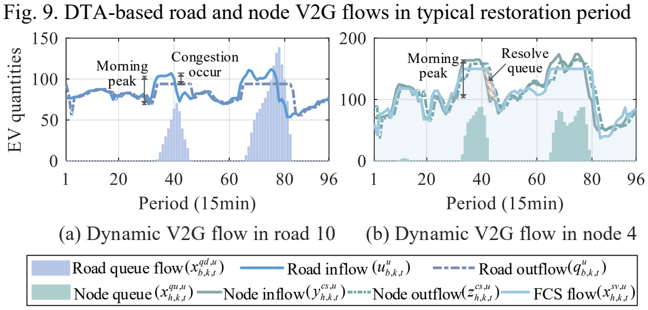

Fig. 10. Analysis of dynamic relationship of queue and EV flow in DTA model

up FCS capacity for upcoming V2G responses.

The time-varying V2G outflow from predecessor roads at each FCS in the UTN, along with the load levels maintained on the PDN buses and surrounding buses, are shown in Fig. 11, focusing on the peak load period (33-66). As seen in Fig. 11, the trends in the maintaining load levels and V2G outflow from predecessor roads are generally aligned, indicating the effectiveness of the proposed V2G response method in load restoration. On the other hand, the V2G outflow from different roads varies significantly over time, even near the same FCS. This variation is due to factors such as traffic assignment in the UTN and road capacities, underscoring the need for coordinated optimization between the PDN and UTN.

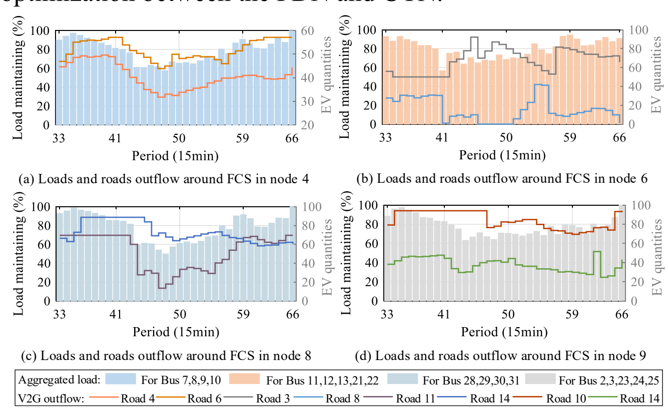

Fig. 11 Critical loads maintaining performance and corresponding road outflows around each FCS

To assess the effectiveness of Cases I-IV in real-time restoration, their computational performance is summarized in Table II. In Cases I and II, the MPC method is set with a rolling horizon of 4 hours, while Case III employs 10 lattices with 50 samples [18]. Among Cases II-IV, Case II has the fastest offline computation due to its single-layer MILP reformulation. Despite sharing a similar DP-based multi-stage structure, Case III's large scenario trees lead to a heavier computational burden, resulting in slower offline performance compared to Case IV. For real-time computation, both Cases III and IV demonstrate significant efficiency as the policy-guided scheme does not require an extended rolling horizon, only needing a single-period problem per restoration interval. Out-of-sample tests further compare the real-time dispatch performance of Cases I-IV, utilizing 1,000 sampled scenarios for DRE and traffic demands through the MC method. The results in Table III show that Cases III and IV substantially outperform the others in total operating cost and load shedding. The period-specific decision policies in these cases effectively address future uncertainties, overcoming the short-sightedness of the MPC-based methods in Cases I and II. Notably, Case IV excels over Case III by more effectively guiding V2G-supporting EVs to address critical loads and mitigate risks from uncertainties, leading to reduced load shedding and lower travel costs for EVs in V2G services. Overall, Case IV exhibits greater robustness, making it more suitable for post-disaster restoration scenarios.

TABLE II
COMPARISON OF OFFLINE AND REAL-TIME COMPUTATIONAL EFFICIENCY ACROSS DIFFERENT CASES ON THE 33P-20U SYSTEM

Case	Offline solution time (sec.)	Real-time computation time/period (sec.)	
		Avg. of all samples	Max. of all samples
I	\	36.096	38.541
II	97.064	39.105	40.032
III	2,521.730	3.425	3.911
IV	836.158	2.039	2.662

TABLE III
COMPARISON OF STATISTIC AVERAGE OUT-OF-SAMPLE PERFORMANCES UNDER DIFFERENT CASES ON 33P-20U SYSTEM

Case	DRE curtailment (10^2\$)	Load shedding (10^4\$)	V2G compensation (10^3\$)	Traveling cost (10^4\$)	Total operation (10^4\$)
I	5.881	8.247	5.352	4.880	12.651
II	3.962	6.337	6.874	3.665	9.355
III	2.503	4.801	6.006	2.086	6.311
IV	3.722	3.054	8.902	4.404	6.605

We conduct numerical experiments to compare the performance of the proposed restoration method under different levels of supporting-V2G EV penetration, with results shown in Table IV. From Table IV, it is evident that while the overall amount of restored load increases with higher EV penetration, the effect of load restoration diminishes when the penetration level becomes too high. This is due to the limitations of FCS capacity and road capacity in the test system. For example, in the +20% case, neither the restored load nor V2G compensation significantly increased. Besides, the excessive increase in EV flow exceeded the system's road capacity, resulting in a sharp rise in travel costs and overall operation costs. These findings highlight the need to dynamically adjust the number of EVs according to the system's capacity to further enhance its resilience.

TABLE IV
PERFORMANCES OF PROPOSED METHOD UNDER DIFFERENT SUPPORTING-V2G EVS PENETRATION

Penetration level	Load shedding (10^4\$)		Avg. V2G compensation (10^3\$)	Avg. traveling cost (10^4\$)	Avg. total cost (10^4\$)
	Avg.	Max.			
+20%	2.573	2.653	9.955	5.150	6.770
+10%	2.681	2.783	9.783	4.692	6.434
Base	3.054	3.212	8.902	4.404	6.605
–10%	3.402	3.632	8.001	4.220	6.856
–20%	3.925	4.260	7.199	3.960	7.195

To validate the restoration performance under varying uncertainty parameters, we examined out-of-sample load shedding on the 33P-20U system in Fig. 12 across adjusted parameters: $\Pi_1^{re(ta)} \in [2:2.5]$, $\Pi_2^{re(ta)} \in [1.5:2.0]$, with a resolution of 0.02. Initially, as the uncertainty parameters increase, restoration improves. However, beyond a certain threshold—specifically when (Π_1^{re}, Π_2^{re}) exceeds (2.16, 1.72) or (Π_1^{ta}, Π_2^{ta}) exceeds (2.38, 1.79)—load shedding increases. This occurs because moderate increases in $\Pi_1^{re(ta)}$ and $\Pi_2^{re(ta)}$ enhance model robustness, but excessively high parameters make the model overly conservative, considering unrealistic scenarios. This premature or over-prepared response can lead to insufficient ramping or V2G EVs congestion, reducing restoration performance. Therefore, selecting appropriate uncertainty parameters is important.

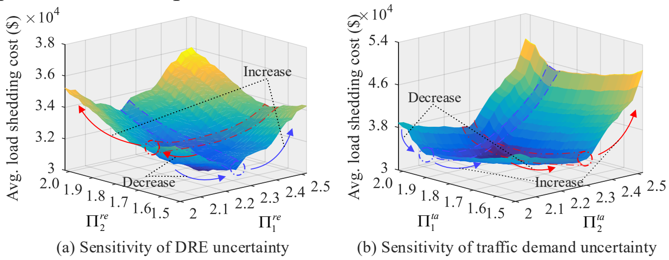

Fig. 12 Sensitivity analysis of uncertainty sets for restoration performance

C. Results of 91P-35U system

The 91-bus PDN and 35-node UTN (91P-35U) system is based on a real-world network in Zhejiang Province, China. The geographical layout of electrical lines and transportation routes is detailed in [37] and simplified in the topology presented in Fig. 13. Disasters have break power supply from all substations, and the damaged lines are highlighted in the figure. Comprehensive system parameters are provided in [37].

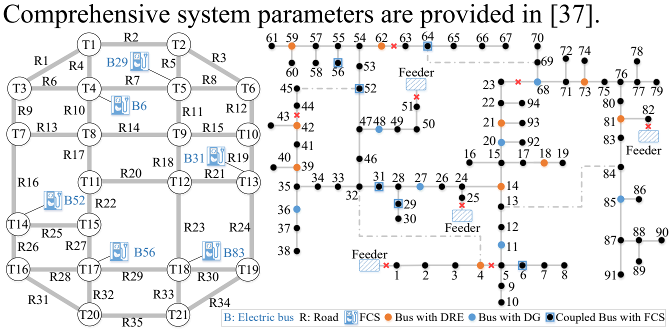

Fig. 13. Topology of 91P-35U system with contingencies

The proposed method achieves convergence of the improved RDDP algorithm's upper and lower bounds to within 0.1% on the 91P-35U system after 1,288 seconds of offline computation, generating real-time restoration policies. Fig. 14 illustrates the in-sample V2G responses and traffic assignments on roads, along with the input marginal price-based compensation for V2G services. From Fig. 14(a) and Fig. 14(b), it is evident that EVs participating in V2G prioritize periods and FCSs offering high compensation prices. The marginal price compensation effectively reflects the power shortages at each bus in the PDN, enabling the restoration method to strategically dispatch V2G EVs to address critical loads in the post-disaster system. Fig. 14(c) and Fig. 14(d) indicate that other vehicles and V2G EVs are overall distributed across different roads to minimize congestion and queuing, facilitating quicker responses from

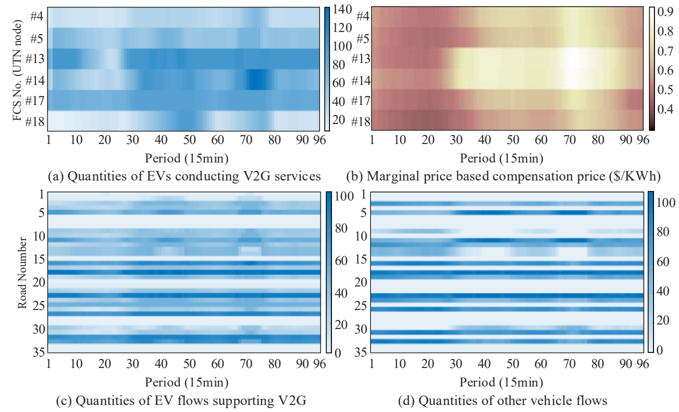

Fig. 14. Traffic assignment in nodes and roads and compensation prices in FCS

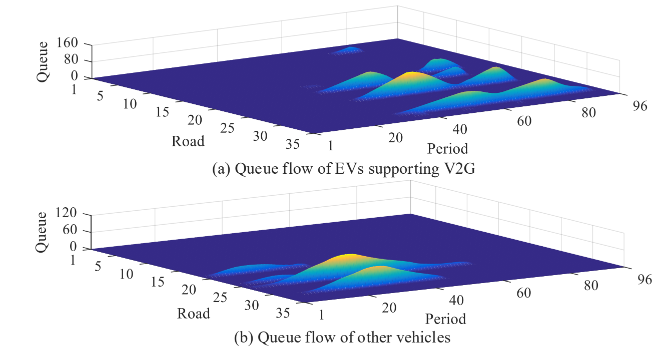

Fig. 15. Traffic assignment in nodes and roads and compensation prices in FCS

V2G-enabled EVs. This demonstrates that the proposed method effectively balances restoration efforts in the PDN with the normal operations of vehicles in the UTN. Moreover, Fig. 15 tracks in-sample queue flow, showing EVs participating in V2G queueing mainly in later periods due to peak compensation prices for load demand, while other vehicles queue earlier. To avoid congestion that could disrupt V2G service and incur penalties from load shedding, non-V2G vehicles take faster routes early to complete O-D tasks, which frees up roads for V2G EVs later.

TABLE V
COMPARISON OF OFFLINE AND REAL-TIME COMPUTATIONAL EFFICIENCY ACROSS DIFFERENT CASES ON THE 91P-35U SYSTEM

Case	Offline solution time (sec.)	Real-time computation time/ period (sec.)		Aggregated real-time computation time/ full- period restoration (sec.)
		Avg. of all samples	Max. of all samples	
I	\	67.085	70.189	5,810.128
II	198.155	69.249	72.650	6,041.323
III	3,806.301	3.903	4.847	339.710
IV	1,287.992	2.582	3.011	224.618

Tables V and VI compare the tractability of Cases I-IV in large-scale systems and their out-of-sample performance during real-time restoration. As shown in Table V, although the iterative solutions required by the DP-based model increase the offline computation time for Cases III and IV, the policy-guided restoration scheme eliminates the additional horizons needed by traditional MPC-based methods to account for future information, significantly enhancing real-time computation speed. In full-period restoration, Cases III and IV require only a few minutes to complete, whereas the MPC-based methods take over an hour. Furthermore, Case IV is faster in both offline and real-time computations because its decision policies encompass only one scenario, while Case III averages multiple

TABLE VI
SPECIFIC COMPARISON OF STATISTIC OUT-OF-SAMPLE PERFORMANCES UNDER DIFFERENT CASES ON 91P-35U SYSTEM

Case	Avg. PDN operation cost (10^3\$)		Avg. UTN operation cost (10^3\$)			Avg. total operation cost (10^3\$)	Avg. total load shedding (KW)	Max. total load shedding (KW)
	DRE curtailment	Load shedding	Node congestion	Road congestion	V2G compensation			
I	6.915	258.260	41.510	89.023	10.990	384.718	25,826.334	32,996.761
II	3.580	214.391	38.089	72.160	12.562	315.658	21,439.126	27,218.905
III	1.156	183.115	20.168	56.982	20.080	241.341	18,311.522	23,896.920
IV	1.903	169.521	29.801	68.544	23.653	246.116	16,952.098	18,282.073

scenario constraints. Table VI presents similar findings to Table III; the out-of-sample results from possible scenarios demonstrate the effectiveness of the proposed method, which more robustly mobilizes flexible resources like V2G responses to pick up critical loads under extreme conditions. Compared to the well-performing existing method, Case III, the proposed method increases critical load restoration by an average of 7.4% and up to 23.49% at maximum.

D. Solution features of improved RDDP

Fig. 16 shows the iteration curves of the improved RDDP algorithm for the 33P-20U and 91P-35U systems, depicting the refinement of upper and lower bounds for problem Q_1. The optimal gap converges to under 0.1% after iterations. For example, the 33P-20U system reaches a gap below 0.5% in about 200 iterations, with full convergence at 331 iterations. This indicates that the convergence criterion confidence levels are allowed to be adjusted for either improved efficiency or higher solution quality, depending on specific needs.

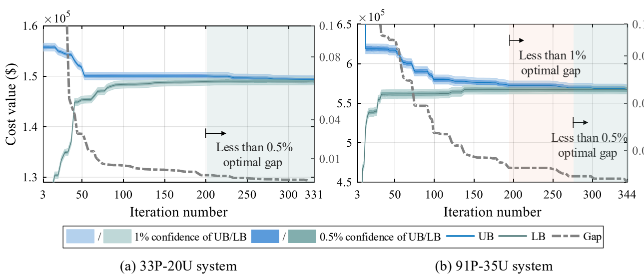

Fig. 16. Offline iteration of improved RDDP algorithm on two test systems

We further compare the average offline lower approximation efficiency at each stage and the backward pass time for Case III and Case IV, as shown in Table VII. For large-scale systems, Lagrangian hyperplane generation takes no more than 0.03 seconds per stage, demonstrating the tractability of the lower approximation. While the improved RDDP method includes an upper approximation, it avoids calculating multiple nodes within scenario tree in SDDiP, which slows down the lower approximation and backward pass in Case III.

TABLE VII
EFFICIENCY COMPARISON OF OFFLINE SOLUTIONS FOR CASE IV AND CASE III IN LOWER APPROXIMATION AND BACKWARD PASS

	Case IV		Case III	
	33P-20U	91P-35U	33P-20U	91P-35U
Avg. each stage L.P. (10^{-2}sec.)	1.941	2.566	21.773	34.892
Aggregated B.P. (sec.)	599.130	912.598	1,864.921	2,721.08

L.P.: Lower approximation; B.P.: Forward/Backward pass

To validate the binarization smoothing technique, we compare the proposed method (with smoothing) to the unsmoothed RDDP method, which uses Benders hyperplanes and LP relaxation for the lower approximation [24], [38], and the convex hull method for the upper approximation. Results show that the unsmoothed RDDP struggles to converge, particularly for the 91P-35U system, with a gap above 10% after 800 iterations, due to non-tight lower and upper bounds for non-convex problems, as detailed in Table VIII.

TABLE VIII
COMPARISON OF ITERATION CHARACTERISTICS FOR SMOOTHING AND NO SMOOTHING IN THE RDDP SOLUTION METHOD

System	Model	Gap (%)	Time (Sec.)	Iteration number
33P-20U	Smoothing	0.083	836.158	331
	Not smoothing	7.044	1,162.559	605
91P-35U	Smoothing	0.091	1,287.992	344
	Not smoothing	10.057	3,034.427	> 800

Furthermore, we compare the proposed scheme (with smoothing) to its not-smoothed counterpart and an ideal dispatch model with perfect forecasts. Testing various penetration levels of supporting-V2G EVs in the 33P-20U system, results in Fig. 17 show that the proposed scheme outperforms the unsmoothed one, with the latter failing to converge and producing suboptimal dispatch policies. While the proposed scheme's maximum optimal gap is around 10%, this is due to both binarization and uncertainties. Moreover, it shows significant improvements in real-time restoration performance and computational efficiency over recent existing studies (Case I-III), highlighting its potential for real-world application.

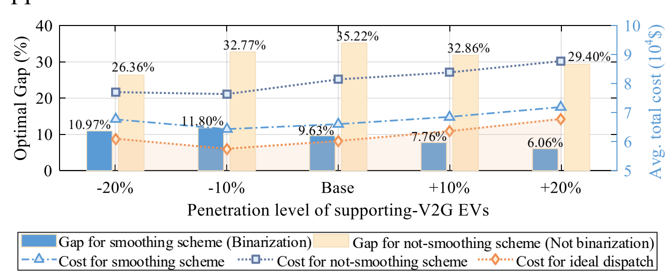

Fig. 17. Solution quality and optimal gap validation for smoothing technique

V. DISCUSSION

(Outages configuration) This study focuses on post-disaster load restoration in the context of PDN line failures [11], but can be easily adapted to scenarios where both PDN lines and UTN roads are affected, such as utility pole collapses. The reason is existing studies typically characterize the impact on UTN roads by reducing their capacity by a certain percentage [39], which only alters input parameters of UTN road capacity without affecting the applicability of the proposed method. Besides, the proposed method addresses load restoration in post-disaster situation, where PDN line outages are predetermined and serve

as input parameters for the proposed model. Therefore, the stochastic of outages is not included in the consideration, as other distribution system restoration studies [9], [24], [40], [41].

(Real-world applicability) The real-world applicability of the V2G mechanism design can be confirmed by: 1) User psychology, where vehicles within the UTN voluntarily participate in V2G-based load restoration without disrupting their normal O-D tasks, making decisions assessing compensation incentives and travel time costs, thus ensuring user autonomy; 2) Literature support, where previous studies [42], [43] similarly adopt V2G compensations for incentivizing load restoration, and studies like [8], [44], [45] emphasizing minimal or no disruption to normal travel plans, though this paper accounts for real-time restoration absent in those studies; and 3) Real-world surveys and cases, where surveys [46], [47], and [48] demonstrate that compensation significantly boosts participation in V2G, while the 2021 Texas winter storm [49] shows users' willingness to engage in load restoration through V2G, and studies from Singapore [50] and Florida practice [51] further confirm that EVs can participate in load restoration while tending to maintain their original travel plans.

(Implications to policy and market design) The proposed V2G restoration method, which incentivizes EV participation through compensation, offers valuable insights for both policy and market design. While no real-world policies currently incentivize EV involvement in V2G during extreme events to enhance grid resilience [42], [52] this study provides a framework for future policy development. In market design, the use of pre-calculated local marginal prices as compensation reflects the power supply status of PDN buses and creates price differentials to adjust V2G incentives. Although more complex market mechanisms, such as game-theoretic models involving power generators and grids, could be developed, we recommend prioritizing straightforward solutions focused on critical load restoration in post-disaster scenarios to ensure social stability.

VI. Conclusion

This paper presents a novel real-time load restoration method that utilizes V2G responses within the coordinated framework of PDN and UTN. The approach features a practical application framework: a DP-based multi-stage RO model is offline formulated to characterize the multi-period restoration under multiple uncertainties, tackled by an improved RDDP algorithm that generates solved value functions for decision-making. In the online application, a single-period scheme efficiently guides real-time load restoration through distributed resources dispatch, network reconfiguration, and V2G assignments, based on these solved value functions. Numerical experiments show that this method effectively overcomes the limitations of traditional MPC-based methods and significantly reduces computation time, completing full-period restoration in minutes compared to over an hour for MPC-based approaches. Moreover, the proposed method enhances out-of-sample critical load restoration by an average of 7.4%, with a maximum improvement of 23.49%.

References

[1] W. Wei, S. Mei, L. Wu, M. Shahidehpour and Y. Fang, "Optimal traffic-power flow in urban electrified transportation networks," *IEEE Trans. Smart Grid*, vol. 8, no. 1, pp. 84-95, Jan. 2017.

[2] X. Chen, X. Wang, M. Shahidehpour, L. Affolabi, Z. Lu and K. Li, "Distributed peer-to-peer coordination of hierarchical three-phase energy transactions among electric vehicle charging stations in constrained power distribution and urban transportation networks," *IEEE Trans. Transp. Electrif.*, vol. 10, no. 2, pp. 4407-4420, Jun. 2024.

[3] S. Lv, Z. Wei, G. Sun, S. Chen, and H. Zang, "Optimal power and semidynamic traffic flow in urban electrified transportation networks," *IEEE Trans. Smart Grid*, vol. 11, no. 3, pp. 1854–1865, May 2020.

[4] H. M. Pennington, C. J. Hanley and J. D. Rogers, "Toward an electromagnetic event resilient grid," *Proc. IEEE*, vol. 109, no. 4, pp. 315-319, Apr. 2021.

[5] J. Li, X. Xu, Z. Yan, H. Wang, M. Shahidehpour and Y. Chen, "Coordinated optimization of emergency response resources in transportation-power distribution networks under extreme events," *IEEE Trans. Smart Grid*, vol. 14, no. 6, pp. 4607-4620, Nov. 2023.

[6] X. Liu, C. B. Soh, T. Zhao, and P. Wang, "Stochastic scheduling of mobile energy storage in coupled distribution and transportation networks for conversion capacity enhancement," *IEEE Trans. Smart Grid*, vol. 12, no. 1, pp. 117–130, 2020.

[7] R. Xu, C. Zhang, D. Zhang, Z. Y. Dong and C. Yip, "Adaptive robust load restoration via coordinating distribution network reconfiguration and mobile energy storage," *IEEE Trans. Smart Grid*, early access, 2024.

[8] B. Li et al., "Routing and scheduling of electric buses for resilient restoration of distribution system," *IEEE Trans. Transp. Electrif.*, vol. 7, no. 4, pp. 2414-2428, Dec. 2021.

[9] L. Zhang, B. Zhang, W. Tang, Y. Lu, C. Zhao and Q. Zhang, "A coordinated restoration method of hybrid AC–DC distribution network with electric buses considering transportation system influence," *IEEE Trans. Ind. Inform.*, vol. 18, no. 11, pp. 8236-8246, Nov. 2022.

[10] B. Li, Y. Chen, W. Wei, S. Huang, Y. Xiong, S. Mei, and Y. Hou,"Routing and scheduling of electric buses for resilient restoration of distribution system," *IEEE Trans. Transp. Electrif.*, vol. 7, no. 4, pp. 2414–2428, 2021.

[11] W. Gan, J. Wen, M. Yan, Y. Zhou, and W. Yao, "Enhancing resilience with electric vehicles charging redispatching and vehicle-to-grid in traffic-electric networks," *IEEE Trans. Ind. Appl.*, vol. 60, no. 1, pp. 953–965, 2024.

[12] S. Yao, P. Wang, X. Liu, H. Zhang and T. Zhao, "Rolling optimization of mobile energy storage fleets for resilient service restoration," *IEEE Trans. Smart Grid*, vol. 11, no. 2, pp. 1030-1043, Mar. 2020.

[13] Y. Tao, J. Qiu, S. Lai, X. Sun, H. Liu and J. Zhao, "Distributed electric vehicle assignment and charging navigation in cyber-physical systems," *IEEE Trans. Smart Grid*, vol. 15, no. 2, pp. 1861-1875, Mar. 2024.

[14] W. u. Rehman, J. W. Kimball and R. Bo, "Multilayered Energy Management Framework for Extreme Fast Charging Stations Considering Demand Charges, Battery Degradation, and Forecast Uncertainties," *IEEE Trans. Transp. Electrif.*, vol. 10, no. 1, pp. 760-776, Mar. 2024.

[15] F. Jiao, Y. Zou, X. Zhang and B. Zhang, "A Three-Stage Multitimescale Framework for Online Dispatch in a Microgrid With EVs and Renewable Energy," *IEEE Trans. Transp. Electrif.*, vol. 8, no. 1, pp. 442-454, Mar. 2022.

[16] Y. Zhou, M. Shahidehpour, Z. Wei, G. Sun and S. Chen, "Multistage robust look-ahead unit commitment with probabilistic forecasting in multicarrier energy systems," *IEEE Trans. on Sustain. Energy*, vol. 12, no. 1, pp. 70-82, Jan. 2021.

[17] Y. Huang, W. Huang, M. Shahidehpour, N. Tai, C. Li and R. Li, "Multistage dispatch of seaport power systems for incorporating logistical flexibilities in uncertain operational conditions," *IEEE Trans. Transp. Electrif.*, vol. 10, no. 3, pp. 6950-6963, Sept. 2024.

[18] A. Papavasiliou, Y. Mou, L. Cambier and D. Scieur, "Application of stochastic dual dynamic programming to the real-time dispatch of storage under renewable supply uncertainty," *IEEE Trans. Sustain. Energy*, vol. 9, no. 2, pp. 547-558, Apr. 2018.

[19] Y. Shi, S. Dong, C. Guo, Z. Chen and L. Wang, "Enhancing the flexibility of storage integrated power system by multi-stage robust dispatch," *IEEE Trans. Power Syst.*, vol. 36, no. 3, pp. 2314-2322, May 2021.

[20] P. Aaslid, M. Korpås, M. M. Belsnes and O. B. Fosso, "Stochastic optimization of microgrid operation with renewable generation and energy storages," *IEEE Trans. Sustain. Energy*, vol. 13, no. 3, pp. 1481-1491, Jul. 2022.

[21] H. Xiong, Y. Shi, M. Shahidehpour, C. Guo and Y. Zhou, "Multi-stage robust optimization of real-time dynamic dispatch with fast-acting units in resilient power systems," *IEEE Trans. Power Syst.*, vol. 40, no. 1, pp. 18- 30, Jan. 2025.

[22] A. Georghiou, A. Tsoukalas, and W. Wiesemann, "Robust dual dynamic programming," *Operations Res.*, vol. 67, no. 3, pp. 813–830, May 2019.

[23] J. Zou, S. Ahmed, and X. A. Sun, "Stochastic dual dynamic integer programming," *Math. Program.*, vol. 175, no. 1, pp. 461-502, May 2019.

[24] L. Wang *et al*., "Enhancing distribution system restoration with coordination of repair crew, electric vehicle, and renewable energy," *IEEE Trans. Smart Grid*, vol. 15, no. 4, pp. 3694-3705, Jul. 2024.
[25] C. Shao, K. Li, T. Qian, M. Shahidehpour and X. Wang, "Generalized user equilibrium for coordination of coupled power-transportation network," *IEEE Trans. Smart Grid*, vol. 14, no. 3, pp. 2140-2151, May 2023.
[26] S. Cai, M. Zhang, Y. Xie, Q. Wu, X. Jin and Z. Xiang, "Hybrid stochastic-robust service restoration for wind power penetrated distribution systems considering subsequent random contingencies," *IEEE Trans. Smart Grid*, vol.13, no. 4, pp. 2859-2872, Jul. 2022.
[27] K. Pang, C. Wang, N. D. Hatziargyriou, F. Wen and Y. Xue, "Formulation of radiality constraints for optimal microgrid formation," *IEEE Trans. Power Syst.*, vol. 38, no. 6, pp. 5341-5355, Nov. 2023.
[28] H. Wang, Y. Ye, Q. Wang, Y. Tang and G. Strbac, "An efficient LP-based approach for spatial-temporal coordination of electric vehicles in electricity-transportation nexus," *IEEE Trans. Power Syst.*, vol. 38, no. 3, pp. 2914-2925, May 2023.
[29] J. Li, X. Xu, Z. Yan, H. Wang, M. Shahidehpour and B. Xie, "Resilient resource allocations for multi-stage transportation-power distribution system operations in hurricanes," *IEEE Trans. Smart Grid*, vol. 15, no. 4, pp. 3994-4009, Jul. 2024.
[30] Y. Chen, S. Hu, S. Xie, Y. Zheng, Q. Hu and Q. Yang, "Optimal dynamic pricing of fast charging stations considering bounded rationality of users and market regulation," *IEEE Trans. Smart Grid*, vol. 15, no. 4, pp. 3950-3965, Jul. 2024.
[31] S. Xie, Y. Xu and X. Zheng, "On dynamic network equilibrium of a coupled power and transportation network," *IEEE Trans. Smart Grid*, vol. 13, no. 2, pp. 1398-1411, Mar. 2022.
[32] V. Gupta et al., "Data-driven models for uncertainty and behavior," Ph.D. dissertation, *Massachusetts Institute of Technology*, 2014.
[33] H. Xiong, Y. Shi, Z. Chen, C. Guo and Y. Ding, "Multi-stage robust dynamic unit commitment based on pre-extended -fast robust dual dynamic programming," *IEEE Trans. Power Syst.*, vol. 38, no. 3, pp. 2411-2422, May 2023.
[34] S. Lv, S. Chen, Z. Wei and G. Sun, "Security-constrained optimal traffic-power flow with adaptive convex relaxation and contingency filtering," *IEEE Trans. Transp. Electrif.*, vol. 9, no. 1, pp. 1605-1617, Mar. 2023.
[35] J. Zou, S. Ahmed and X. A. Sun, "Multistage stochastic unit commitment using stochastic dual dynamic integer programming," *IEEE Trans. Power Syst.*, vol. 34, no. 3, pp. 1814-1823, May 2019.
[36] L. Shbeeb, "The relation between transit service availability and productivity with customers satisfaction," *Transportation Research Interdisciplinary Perspectives*, vol. 16, pp. 100716, 2022.
[37] Data of 33P-12U and 91P-35U systems. [Online]. Available: https://drive.google.com/file/d/1qiJqpC-Vmpl85rxDCNkTQOxGYfY-L5t2/view?usp=sharing
[38] M. N. Hjelmeland, J. Zou, A. Helseth and S. Ahmed, "Nonconvex medium-term hydropower scheduling by stochastic dual dynamic integer programming," *IEEE Trans. Sustain. Energy*, vol. 10, no. 1, pp. 481-490, Jan. 2019.
[39] J. Wen, W. Gan, C. -C. Chu, L. Jiang and J. Luo, "Robust resilience enhancement by EV charging infrastructure planning in coupled power distribution and transportation systems," *IEEE Trans. Smart Grid*, vol. 16, no. 1, pp. 491-504, Jan. 2025.
[40] J. Li, X. Xu, H. Wang, Z. Yan, M. Shahidehpour and B. Yang, "Coordinated multi-task scheduling of electric buses in post-disaster transportation-power distribution systems," *IEEE Trans. Transp. Electrif.*, early access, 2024, DOI: 10.1109/TTE.2024.3504855.
[41] Z. Liu, Q. Wu, X. Shen, J. Tan and X. Zhang, "Post-disaster robust restoration scheme for distribution network considering rerouting process of cyber system with 5G," *IEEE Trans. Smart Grid*, vol. 15, no. 5, pp. 4478-4491, Sept. 2024.
[42] M. Reza Salehizadeh *et al*., "Preventive energy management strategy before extreme weather events by modeling EVs' opt-in preferences," *IEEE Trans. Intell. Transp.*, vol. 25, no. 11, pp. 18368-18382, Nov. 2024.
[43] R. Bayani and S. Manshadi, "An agile mobilizing framework for V2G-enabled electric vehicles under wildfire risk," *IEEE Trans. Veh. Technol.*, early access, 2024. DOI: 10.1109/TVT.2024.3508671.
[44] L. Kong, H. Zhang, D. Xie and N. Dai, "Leveraging electric vehicles to enhance resilience of interconnected power-transportation system under natural hazards," *IEEE Trans. Transp. Electrif.*, early access, 2024, DOI: 10.1109/TTE.2024.3400289.
[45] Y. Li, D. Zhang, J. Zhu, K. W. Cheung and S. Li, "Resilience enhancement in urban power-transportation system considering multiple uncertainties against ice storms," *IEEE Trans. Smart Grid*, vol. 16, no. 1, pp. 801-815, Jan. 2025.
[46] J. Owens, I. Miller, and E. Gencer, "Can vehicle-to-grid facilitate the transition to low carbon energy systems?" *Energy Adv.*, vol. 1, no. 12, pp. 984-998, 2022.
[47] J. Geske and D. Schumann, "Willing to participate in vehicle-to-grid (V2G)? Why not!" *Energy Policy*, vol. 120, pp. 392-401, Sep. 2018.
[48] M. Mehdizadeh, T. Nordfjaern, and C. A. Klockner, "Estimating financial compensation and minimum guaranteed charge for vehicle-to-grid technology," *Energy Policy*, vol. 180, Sep. 2023, Art. no. 113649.
[49] *Reversing the Charge—Battery Power From Electric Vehicles to the Grid Could Open a Fast Lane to a Net-Zero Future*. Accessed: Nov. 7, 2022. [Online]. Available: https://energy.mit.edu/news/reversing-the-charge/
[50] G. Raman, G. Raman, and J. CH. Peng. "Resilience of urban public electric vehicle charging infrastructure to flooding," *Nat. Commun.*, vol. 13, p. 3213, Jun. 2022.
[51] C. Johnson *et al*, *Florida Alternative Transportation Fuel Resilience Plan*, 2022.
[52] A. Hussain and P. Musilek, "Resilience enhancement strategies for and through electric vehicles," *Sustain. Cities Soc.*, vol. 80, pp. 103788, May 2022.

Houbo Xiong (Student Member, IEEE) received his B.Sc. degree in the College of Electrical Engineering at Hubei University of Technology, Wuhan, China, in 2021. He is currently working toward the Ph.D. degree with the College of Electrical Engineering, Zhejiang University. From 2024 to 2025, he was a visiting scholar with Nanyang Technological University, Singapore. His research interests include renewable power system optimization, power-traffic coordination, and grid resilience.

Yan Xu (Senior Member, IEEE) received the B.E. and M.E degrees from the South China University of Technology, Guangzhou, China, in 2008 and 2011, respectively, and the Ph.D. degree from the University of Newcastle, Callaghan, NSW, Australia, in 2013. After the postdoctoral training with the University of Sydney Postdoctoral Fellowship, he joined Nanyang Technological University (NTU) with the Nanyang Assistant Professorship. He was promoted to Associate Professor in 2021 and appointed as the Cham Tao Soon Professor in engineering (an endowed professorship named after the founding president of NTU) in 2024. At NTU, he is currently the Director of Center for Power Engineering, and the Co-Director of SingaporePower Group–NTU Joint Lab. His research interests include power system stability and control, microgrids, and data-analytics for smart grid applications. Dr Xu was the recipient of the Nanyang Research Award (Young Investigator) by NTU, and the Outstanding Engineer Award by IEEE Power & Energy Society (PES) Singapore Chapter. Dr Xu's professional service roles include an Associate Editor for IEEE TRANSACTIONS SMART GRID and IEEE TRANSACTIONS POWER SYSTEMS, Chairman of IEEE PES Singapore Chapter (2021 and 2022), and the General Co-Chair of the 11th IEEE ISGT-Asia Conference in 2022.

Zhao Yang Dong (Fellow, IEEE) received the Ph.D. degree in electrical engineering from the University of Sydney, Sydney, Australia, in 1999. He is currently the Head of Department and a Chair Professor of Electrical Engineering with the City University of Hong Kong, Hong Kong. His previous roles include a SHARP Professor of Energy Systems and an inaugural Director of the UNSW Digital Grid Futures Institute, The University of NSW, Sydney; the Director of the ARC Research Hub for Integrated Energy Storage Systems; the Head of the School of Electrical and Information Engineering, The University of Sydney; and the Ausgrid Chair Professor and the Director of the Ausgrid Centre for Intelligent Electricity Networks providing research and development support for the AUD500m Smart Grid, Smart City National Demonstration Project of Australia. His research interests include power system planning and stability, smart grids and smart cities, renewable energy systems, and energy market. He has been serving as an editor/associate editor for a number of IEEE TRANSACTIONS and IET journals.

Wei Gan (Member, IEEE) received the B.S. and Ph.D. degrees in electrical engineering from the Huazhong University of Science and Technology, Wuhan, China, in 2016 and 2021, respectively. From 2018 to 2019, he was a Visiting Ph.D. Student with the China Electric Power Research Institute, Beijing, China. From 2019 to 2020, he was a Visiting Ph.D. Student with the Robert W. Galvin Center for Electricity Innovation, Illinois Institute of Technology, Chicago, IL, USA. He is currently a Postdoctoral Research Associate with the School of Engineering, Cardiff University, Cardiff, U.K. His research interests include peer-to-peer energy trading, coordinated optimization of power-traffic systems, and multiple energy system integration.

Chuangxin Guo (Senior Member, IEEE) received the Ph.D. degree in Electrical Engineering from Huazhong University of Science and Technology, Wuhan, China, in 1997. He is currently a Professor with the College of Electrical Engineering, Zhejiang University, Hangzhou, China. Prior to joining Zhejiang University, he was the Director of Beijing Dongfang Electronics Research Institute. His research interests include power system operation and planning, and power systems information and communication technologies.

Mingyu Yan (Member, IEEE) received the B.S. degree from the College of Electrical Engineering, Zhejiang University, Hangzhou, China, in 2016, the M.S. degree from the Huazhong University of Science and Technology, Wuhan, China, in 2018, and the Ph.D. degree from the Robert W. Galvin Center for Electricity Innovation, Illinois Institute of Technology, Chicago, IL, USA, in 2021. From 2021 to 2022, he was a Research Associate with Imperial College London, London, U.K. He is currently a Full Professor with the School of Electrical and Electronics Engineering, Huazhong University of Science and Technology. His research interests include power market, peer-to-peer energy trading, virtual power plants, multiple energy system integration, and renewable energy.